High-Resolution Monte-Carlo Simulation of Flow and Conservative Transport in Heterogeneous Porous Media: 2, Transport Results

R.L. Naff

U.S. Geological Survey

Water Resources Division

Denver, Colorado, USA

D.F. Haley

Waterloo Centre for Groundwater Research

University of Waterloo

Waterloo, Ontario, Canada

E.A. Sudicky

Waterloo Centre for Groundwater Research

University of Waterloo

Waterloo, Ontario, Canada

August, 1996

Revised June, 1997

Abstract

In this second of two papers concerned with the use of numerical simulation to examine flow and transport parameters in heterogeneous porous media via Monte-Carlo methods, results from the transport aspect of these simulations are reported on. Transport simulations contained herein assume a finite pulse input of conservative tracer, and the numerical technique endeavors to realistically simulate tracer spreading as the cloud moves through a heterogeneous medium. Medium heterogeneity is limited to the hydraulic conductivity field, and generation of this field assumes that the hydraulic-conductivity process is second-order stationary. Methods of estimating cloud moments, and the interpretation of these moments, are discussed. Techniques for estimation of large-time macrodispersivities from cloud second-moment data, and for the approximation of the standard errors associated with these macrodispersivities, are also presented. These moment and macrodispersivity estimation techniques were applied to tracer clouds resulting from transport scenarios generated by specific Monte-Carlo simulations. Where feasible, moments and macrodispersivities resulting from the Monte-Carlo simulations are compared with first- and second-order perturbation analyses. Some limited results concerning the possible ergodic nature of these simulations, and the presence of non-Gaussian behavior of the mean cloud, are reported on as well.

Introduction

In this second of two papers on simulation of conservative transport in heterogeneous media by Monte-Carlo (MC) techniques, the principal results from these simulations are reported on. In the first paper [*Naff et al.*, this issue] the model and modelling techniques involved in these simulations are discussed, as well as some of the initial results concerning the velocity field and mean travel time of the tracer cloud. In this second paper, we devote our effort to analyzing cloud moments greater than one; we are principally interested in measures of the macrodispersion which result from these simulations. The ergodicity of these clouds, as measured by the reduction in the variance of a moment, is also touched on, as wells as the expected skewness of the tracer cloud.

Previously, a more limited multirealization analysis [*Burr et al.*, 1994] was used to conduct a preliminary investigation of both reactive and nonreactive transport in heterogeneous porous media; the numerical model and random field generator used in this earlier study were extensively revised for this study, and the scope of the investigation, for conservative tracers, enlarged. Although a number of other investigators have published studies of transport in heterogeneous media using random fields and numerical models, few studies model actual three-dimensional transport through heterogeneous porous media; those that do [*Tompson and Gelhar*, 1990; *Tompson*, 1993; *Jussel et al.*, 1994] consider only a limited number of realizations for each transport scenario considered. Many simulations of transport through heterogeneous porous media employ particle tracking schemes rather than complete models of plume development [*Chin and Wang*, 1992; *Bellin et al.*, 1992]. While these simulations do lend themselves well to the MC simulation technique, they do so at the expense of eliminating explicit local dispersive effects from the simulations; impicit effects, in the form of numerical dispersion, may be present in these simulations but are more difficult to independently quantify [*Harter and Yeh*, (1996)]. Generally

speaking, results from MC simulations using particle tracking schemes tend to agree rather well with first-order analytical results where local dispersion is neglected (in particular, those results presented by *Dagan* [1984, 1987, 1988]). The present study is rather minimal in the number of realizations used ($\sim$ 20) but includes local dispersion effects; this compromise was necessary if a significant number of different MC scenarios were to be run. In this report, we will make selective comparisons with analytical results from work by *Dagan* [1984, 1988], *Gelhar and Axness* [1983], *Naff* [1990, 1994], and *Zhang and Neuman* [1990]. This is not to imply that these are the only, or most valuable analytical results available; investigations by many others certainly contribute [e.g., *Sposito and Barry*, 1987; *Zhang*, 1995]. However, we found the results given in these select works either most useful or most readily available (i.e., in a closed form) in comparison with other works.

Two problem areas became evident in the course of performing and then reducing the data from these simulations. The first difficulty has to do with the number of realizations used in these simulations. The number of realizations, N_r, necessary to obtain a stable representation of the mean spatial moment increases with the order of the moment; that is, the variability in the mean of the first moment, or plume centroid, is less than that of the second-central moment. This phenomenon probably results because the higher moments are more profoundly influenced by the tail behavior of the tracer clouds. Our observation is that on the order of 20 realizations is necessary to obtain reasonably consistent behavior on the part of the second-central moment; that is, with approximately 20 realizations, the addition of yet another realization will have a minimal influence on the overall mean. However, we did not attempt, in these simulations, to use realizations in numbers sufficient to remove all variability from the mean second moment. The reason for this is simply that the standard deviation of the mean estimator decreases as the inverse of the square root of the number of realizations: $1/\sqrt{N_r}$. Thus, to decrease the variability in the mean estimator by a factor of two, the number of realizations run would have had to be

increased by a factor of four; this was not computationally feasible given the number of scenarios that we wished to examine.

The second and related difficulty has to do with determining when asymptotic behavior of the mean, second-central spatial moments begins in these 20 realization simulations. Here, asymptotic behavior is defined as the stable, late-time moment behavior in which the moment is a linearly increasing function of time. For reasons that are not entirely clear, the onset of asymptotic behavior in, for example, the mean longitudinal variance of the cloud can be highly variable from MC simulation to MC simulation. In particular, for these 20 realization simulations the onset of linear behavior of the second moments appears to have been sensitive to the set of realizations selected for a particular MC simulation. Because macrodispersion coefficients used in this study are based on this asymptotic linear behavior, being able to define its onset become rather critical. The net results of this variability as well as the general variability of the second moments mentioned in the previous paragraph is that, in some instances, it became difficult to determine which segment of the mean curve best represented the macrodispersivity. For our macrodispersivity approximations, we attempted to select the largest practical interval where the mean variance curves exhibits linearity in late time. Generally, four or more data points were used in determining macrodispersivities; cases where fewer points were used are discussed in detail in the pertinent sections of this report.

In the next section, we review the basis of our MC simulations as well as the various scenarios to be covered in this report. An extensive discussion of the development of measures for the mean and variance of the cloud moments, as well as the mean and variance in macrodispersivities, is presented in the subsequent two sections. The measures put forth in these sections are the basis for much of the discussion presented throughout this report. Subsequently, the dependence of macrodispersion on the medium variance and length

scales, as well as local dispersion is discussed over several sections. Two sections devoted to the discussion of ergodic and cloud development follow; lastly, a brief discussion of the expected skewness of the mean cloud is presented.

Monte-Carlo Scenarios

This modelling effort consists of numerical simulation of the movement of a hypothetical conservative tracer through a heterogeneous hydraulic conductivity field; a spectral scheme was used to generate heterogeneous fields which, because of the assumed second-order stationarity, are characterized by length scales and a variance. A realization of a random velocity field was created by forcing a head differential across a parallelepiped containing the generated hydraulic conductivity field. The tracer source was modelled as a small finite pulse near the upgradient end of the parallelepiped enclosing the flow domain; the modelling effort produced high-quality simulations of the transport of this pulse through the random velocity field. As noted in the first paper [*Naff et al.*, this issue], the realization hydraulic conductivity associated with the source box was conditioned so as to conserve on modelling domain. Raw moments were estimated from these tracer clouds for travel distances ranging from one to two length scales to a maximum of about twelve length scales. These transport simulations were repeated for new realizations of the hydraulic conductivity field, and the estimated raw cloud moments were collected for each realization; about 20 realizations were used in a typical MC simulation. The term "Monte-Carlo scenario" is used here to denote a MC simulation run for a specific set of statistical and physical parameters.

With varying success, we attempted several scenarios in which one variable (medium statistic, transport parameter) was isolated to ascertain its effects on cloud development. The medium parameters investigated are the estimated variance in the logarithm of the hydraulic conductivity, $\hat{\sigma}_f^2$, and the estimated length scales in the x, y and z directions: $\hat{\lambda}_x$, $\hat{\lambda}_y$ and $\hat{\lambda}_z$. The transport parameters consist of the local transverse dispersivity α_t and the vertical dimension of the initial source I_z; the local longitudinal dispersivity α_ℓ was held constant at $0.1\ m$ for all simulations. These scenarios are listed in Table 1. The source size in the x and y directions for all scenarios was a small fraction of the length scales in these directions, depending on the discretiztion used in each scenario. In the case of first scenario,

for example, $I_x = 0.24\hat{\lambda}_x$ and $I_y = 0.18\hat{\lambda}_y$; this is typical of the other scenarios as well. It was our goal with these MC simulations to obtain 20 realizations in which the minimum travel distance of the individual plume centroids was on the order of ten length scale $\hat{\lambda}_x$. This goal was not always obtained, particularly in the case of scenario two; instances where significant deviation from this objective occurred will be cited in the following discussion. Of these scenarios, the first, where the variance in the logarithm of the hydraulic conductivity, σ_f^2, is varied, was perhaps the most successful in that little difficulty was encountered in translating these results into macrodispersivities. Scenarios two and four, on the other hand, were among the most difficult to consistently interpret for reasons which will be given subsequently; the results from these two scenarios are among the most problematic for this study. The interpretation of results from the remaining scenarios generally did not present the problems encountered in scenarios two and four but were seldom as straight forward as those of the first scenario.

Estimation of Cloud Spatial Moments

Spatial moments for the concentration clouds are obtained from standard formulae for raw moments $M_{ijk}(t)$:

$$M_{ijk}(t) \;=\; \frac{m_{ijk(t)}}{m_{000}} \tag{1}$$

where the unscaled moments, $m_{ijk}(t)$, are defined as

$$m_{ijk}(t) \;=\; \int_{-\infty}^{\infty}\int_{-\infty}^{\infty}\int_{-\infty}^{\infty} x^i y^j z^k C(\vec{x},t)\; d\vec{x}$$

Note that m_{000} represents the mass of the cloud. The concentration $C(\vec{x},t)$ can represent either the average concentration field or the concentration cloud from a single realization. The unscaled moments $m_{ijk}(t)$ are obtained by piecewise integration over the finite element mesh; the concentration $\hat{C}_e(\vec{x},t)$ within a hexahedral element e is approximated with trilinear shape functions $\phi_q(\vec{x})$ as

$$\hat{C}_e(\vec{x},t) \;=\; \sum_{q=1}^{8} \phi_q(\vec{x})\, C(\vec{x}_q,t) \tag{2}$$

where $C(\vec{x}_q,t)$ is the concentration at nodal location $\vec{x}_q$ of element e as determined by the Galerkin-Laplace transform solution technique for the transport problem (see *Desai and Abel* [1972, Table 5-1] for the definition of shape functions $\phi_q(\vec{x})$). For element e the unscaled moment contribution becomes

$$m^e_{ijk}(t) \;=\; \int_{x_n}^{x_{n+1}}\int_{y_m}^{y_{m+1}}\int_{z_p}^{z_{p+1}} x^i y^j z^k \hat{C}_e(\vec{x},t)\, d\vec{x} \tag{3}$$

where element e is defined by mesh coordinates $x_n \le x \le x_{n+1}, y_m \le y \le y_{m+1}, z_p \le z \le z_{p+1}$. Summation of $m^e_{ijk}(t)$ over all elements N_e results in an estimate of the unscaled moment $m_{ijk}(t)$ for the cloud simulation in question:

$$m_{ijk}(t) \;=\; \sum_{e=1}^{N_e} m^e_{ijk}(t) \tag{4}$$

Upon substitution of (2) into (3) and interchanging integration with summation, the unscaled moments $m^e_{ijk}(t)$ becomes a weighted summation over the nodal concentrations of the elements:

$$m^e_{ijk}(t) \;=\; \sum_{q=1}^{8} w^q_{ijk}\, C(\vec{x}_q, t) \tag{5}$$

The weights w^q_{ijk} are defined from the integral expression

$$w^q_{ijk} \;=\; \int_{x_n}^{x_{n+1}} \int_{y_m}^{y_{m+1}} \int_{z_p}^{z_{p+1}} x^i y^j z^k \phi_q(\vec{x})\, d\vec{x} \tag{6}$$

Expressions (1), (4), (5) and (6) were used to the evaluate raw moments in this study. The central moments μ_{ijk}, defined as

$$\mu_{ijk}(t) \;=\; \frac{1}{m_{000}} \int_{-\infty}^{\infty} \int_{-\infty}^{\infty} \int_{-\infty}^{\infty} (x - M_{100})^i (y - M_{010})^j (z - M_{001})^k C(\vec{x}, t)\; d\vec{x} \tag{7}$$

can be expressed in terms of the raw moments $M_{ijk}(t)$; for the case where the exponents i, j. k are greater than unity, these expressions result by expansion of the binomials in (7).

The above formulae can be applied to a single realization of the concentration field, denoted herein as $C_\ell(\vec{x}, t)$, or to the mean concentration field $\langle C(\vec{x}, t) \rangle$, obtained by averaging the individual clouds over all realizations N_r:

$$\langle C(\vec{x}, t) \rangle \;=\; \frac{1}{N_r} \sum_{\ell=1}^{N_r} C_\ell(\vec{x}, t)$$

When applied to the mean concentration, the resulting first moments will be denoted as $\hat{M}_{ijk}$, where $i,j,k = 0,1$, and second central moments as $\hat{\mu}_{ijk}$, where $i,j,k = 0,2$; first cross moments, where $i+j+k > 1$, and second central cross moments, where $i+j+k > 2$, will not be considered in this study. When applied to the concentration field from a single realization, the first moments will be denoted as M_{ijk}, where $i,j,k = 0,1$, and second central moments as μ_{ijk}, where $i,j,k = 0,2$; in the event a specific realization ℓ is to be indicated, then this symbol will be added to the subscript: $M_{ijk(\ell)}$ and $\mu_{ijk(\ell)}$. With regard to the first moments, the following relation holds:

$$\langle M_{ijk} \rangle \;=\; \frac{1}{N_r} \sum_{\ell=1}^{N_r} M_{ijk(\ell)} \;\approx\; \hat{M}_{ijk}$$

where N_r is the number of realizations and $i,j,k = 0,1$; that is, the average of these moments over realizations are very nearly identical to the mean-cloud moments. These moments would be identical except for the slight variation in the mass m_{000} from realization to realization. These small variations in m_{000}, reflecting the inability of the numerical procedure to exactly resolve the concentration cloud, are largely insignificant to these results. For the purposes of this study, these first moments will be considered to be identical: $\hat{M}_{ijk} \equiv \langle M_{ijk} \rangle$, where $i,j,k = 0,1$. The same is not true for the second central moments; that is,

$$\langle \mu_{ijk} \rangle \;=\; \frac{1}{N_r} \sum_{\ell=1}^{N_r} \mu_{ijk(\ell)} \;\not\equiv\; \hat{\mu}_{ijk}$$

where $i,j,k = 0,2$. In general, the notation $\langle \cdot \rangle$ will be used to represent a sample mean across realizations.

These formulae for moments can be used to illustrate some important concepts concerning moments; in particular, that the variance of the mean cloud is greater than the mean of the variances of the individual clouds. To show this, we replace the concentration field $C(x,t)$ in (1) with the mean concentration over N_r realizations such that:

$$\hat{m}_{ijk}(t) \;=\; \int_{-\infty}^{\infty}\int_{-\infty}^{\infty}\int_{-\infty}^{\infty} x^i y^j z^k \langle C(\vec{x},t)\rangle \; d\vec{x} \tag{8}$$

In accord with (1), we consider that $\hat{m}_{000}(t) = \langle m_{000}(t)\rangle \approx m_{000}$; that is, the mass of the cloud is constant. Allowing $f_\ell(\vec{x},t) = C_\ell(\vec{x},t)/m_{000}$ to represent the relative frequency of a single cloud, then the ensemble mean second central moment for the x direction, for example, becomes

$$\hat{\mu}_{200}(t) \;=\; \int_{-\infty}^{\infty}\int_{-\infty}^{\infty}\int_{-\infty}^{\infty} (x-\hat{M}_{100})^2 \langle f(\vec{x},t)\rangle \; d\vec{x} \tag{9}$$

where

$$\langle f(\vec{x},t)\rangle \;=\; \frac{1}{N_r}\sum_{\ell=1}^{N_r} f_\ell(\vec{x},t)$$

Note that the mean-cloud central moment is defined with respect to $\hat{M}_{100}(t)$ which, except for the slight variation in m_{000} through the numerical solution, is identical to $\langle M_{ijk}\rangle$. By interchanging summation and integration in (9) and rewriting the integrand as

$$\hat{\mu}_{200}(t) \;=\; \frac{1}{N_r}\sum_{\ell=1}^{N_r}\int_{-\infty}^{\infty}\int_{-\infty}^{\infty}\int_{-\infty}^{\infty} \Big[(x-M_{100(\ell)}) - (\hat{M}_{100}-M_{100(\ell)})\Big]^2 f_\ell(\vec{x},t)d\vec{x}$$

one obtains the result

$$\hat{\mu}_{200}(t) \;=\; \langle \mu_{200}\rangle + S_{200} \tag{10}$$

where

$$\langle \mu_{200}\rangle \;=\; \frac{1}{N_r}\sum_{\ell=1}^{N_r} \mu_{200(\ell)} \tag{11a}$$

$$S_{200} \;=\; \frac{1}{N_r}\sum_{\ell=1}^{N_r} \big(M_{100(\ell)} - \langle M_{100}\rangle\big)^2 \tag{11b}$$

The symbol S_{200} denotes the variance of the cloud centroid about its mean in the x direction; note that this definition for the variance of the cloud centroid can be extended to the y and z directions: S_{020} and S_{002}. Expression (10) makes clear that $\hat{\mu}_{200}(t)$ differs from $\langle \mu_{200} \rangle$ by the variance in the x-direction cloud centroid; unless S_{200} is zero, $\hat{\mu}_{200}(t)$ will always be larger than $\langle \mu_{200} \rangle$. This result, although not new, is significant in that most analytical approximations of the second central moment are based on the mean concentration field.

Determination of Macrodispersivities and Standard Errors

Macrodispersivities and macrodispersion coefficients are determined from the slope of the late-time portion of the second-moment curves μ_{200}, μ_{020} and μ_{002}. For the first MC scenario where $\hat{\sigma}_f^2 = 0.524$ and $\hat{\lambda}_x = 2.78\,m$, $\hat{\lambda}_y = 2.79\,m$, $\hat{\lambda}_z = 0.278\,m$, a typical set of second central moments μ_{200} from a 20 realization MC simulation is shown in Figure 1; the mean of these moments, as determined from the 20 realizations, is also depicted in this figure. As the behavior of $\langle\mu_{200}\rangle$ in the interval between 100 and 280 days is relatively linear, it is possible to obtain an estimate, from the slope of a straight-line fit to second-moment data within this time interval, for the mean effective longitudinal dispersion coefficient $\langle D_{xx}\rangle$. Note that information from day 300 is not used to estimate this mean slope as the number of realizations represented in the mean decreases to 19 for this time; this decrease is the result of a plume realization encountering the detection boundary at the time step corresponding to day 300 (for this case $\langle V_c\rangle = 0.098\ m/d$ and $t\langle V_c\rangle/\hat{\lambda}_x = 9.9$ for 280 days of travel time). Also, because the value of $\langle\mu_{200}\rangle$ at times less than 80 days indicates that these mean moments may yet contain some early time behavior, they were eliminated.

The selection of late-time segments of the second-moment curves $\langle\mu_{200}\rangle$, $\langle\mu_{020}\rangle$ and $\langle\mu_{002}\rangle$ for the purpose of estimating their slopes and determining mean coefficients $\langle D_{xx}\rangle$, $\langle D_{yy}\rangle$ and $\langle D_{zz}\rangle$ is subjective. When the late-time segments are rather straight, as indicated in Figure 1, then this subjectivity has only a minor effect on the resulting estimates of the macrodispersion coefficients. However, because these second-moment curves are the mean of at most 20 realizations, they can yet contain unexpected wiggles, even in late time. Two of the more common variants of these curves are shown in Figure 2, where curves with other than largely straight-line behavior in mid to late time are illustrated. These second-moment curves were obtained from two MC simulations with different sets of random hydraulic-conductivity realizations and do not correspond to any particular MC

scenario cited in this study; the local transverse dispersivity of example A is twice that of B, but otherwise these simulations share the same input parameters. The $\langle\mu_{200}\rangle$ curve for A exhibits a region of downward convexity at about 150 days, while B exhibits upward convexity at about 175 days. The opposite relation is to be observed in $\langle\mu_{020}\rangle$ (and to a lesser degree, in $\langle\mu_{002}\rangle$ as well), where A is convex upward and B is convex downward. This opposing relation was generally observed: should $\langle\mu_{200}\rangle$ have an unusual bow, then either $\langle\mu_{020}\rangle$ or $\langle\mu_{002}\rangle$ (or both) would have an opposing bow. For individual realizations, this tendency for the second-moment curves to bow in late time is related to the hydraulic conductivity configuration encountered by the tracer fluid downgradient of the initial zone; these mean curves represent the cumulative effect of this tendency. In general, if these wiggles were small, we tended to ignore them and use as much of the curve as possible for the purpose of estimating the slope. However, bows such as that exhibited in example A were not easily ignored, in large part because it became difficult to discern initial and asymptotic behaviors of the second-moment curves. In these cases, our conservative selection technique may have caused us to overestimate the longitudinal component and underestimate the transverse components of the macrodispersion tensor.

From Figure 1 it is also apparent that individual second-moment realizations μ_{200} exhibit considerable variability, both between realizations and temporally within a realization. To evaluate the effect of interrealization variability in μ_{200} on the effective macrodispersion coefficient, the same time interval as used to capture the mean effective coefficient from the mean variance $\langle\mu_{200}\rangle$ can be applied to individual realizations; that is, longitudinal variance data for each realization in the 100 to 280 day interval is fit with a straight line and the slope, $S_{x\ell}$, of that line is assumed to represent the effective dispersion coefficient for realization ℓ. Given that the effective coefficient for a single realization is

$D_{xx(\ell)} = S_{x\ell}/2$, mean and variance statistics for the effective longitudinal dispersion coefficient D_{xx} can be determined from this slope information. The mean effective dispersion coefficient, $\langle D_{xx} \rangle$, estimated by this technique, is identical to that obtained by fitting a straight line directly to the mean longitudinal variance $\langle \mu_{200} \rangle$ of Figure 1 and using the slope of this line as an estimate of the mean dispersion coefficient. As the realizations are all independent, the variance of $\langle D_{xx} \rangle$ is simply $\sigma^2_{D_{xx}}/N_r$ where $\sigma^2_{D_{xx}}$ is the variance in D_{xx} and N_r is the number of realizations in the MC simulation. Given an estimate $\hat{\sigma}^2_{D_{xx}}$ for the variance in D_{xx}, the standard error of $\langle D_{xx} \rangle$ can be approximated as $\hat{\sigma}_{D_{xx}}/\sqrt{N_r}$ where, for the example given in Figure 1, $N_r = 20$. Thus, a measure of the error involved in estimating the mean effective macrodispersion coefficients is obtained by this procedure. Note that, as N_r increases, the standard error $\hat{\sigma}_{D_{xx}}/\sqrt{N_r}$ decreases and the mean dispersion coefficient is better determined. The mean and standard errors for the transverse coefficients, D_{yy} and D_{zz}, are similarly determined. While this technique captures the general interrealization variability of the effective macrodispersion coefficient for a particular interval, it tends to smooth the temporal variability within each realization moment. As noted for the velocity estimates in the companion paper [*Naff et al.*, this issue], when the interval upon which this variance estimate is based becomes smaller, the variance itself becomes larger; this results as less temporal smoothing of the second moment is obtained by using smaller intervals. In the case of Figure 1, if the effective macrodispersion coefficient is based on the minimum interval of 20 days (every two values of $\mu_{200}(t)$), then the estimated variance $\hat{\sigma}^2_{D_{xx}}$ is about twice that obtained from the much larger interval of 200 days. Thus, one should be aware that these estimates of the variance in $D_{xx(\ell)}$ are not without their problems; they are used in this study as being indicative of the variance that one might expect from this type of experiment.

With respect to the mean cloud $\langle C(\vec{x},t)\rangle$, macrodispersion coefficients $\langle E_{xx}\rangle$, $\langle E_{yy}\rangle$ and $\langle E_{zz}\rangle$ and their standard errors can be determined in a similar manner from cloud second moments $\hat{\mu}_{200}$, $\hat{\mu}_{020}$ and $\hat{\mu}_{002}$. From (9) one can obtain an expression for the second central moment with respect to the realization mean centroid $\langle M_{ijk}\rangle$, $i,j,k = 0,1$, for every cloud realization. For example, the second moment $\mu'_{200(\ell)}$ for realization ℓ in the x direction with respect to the realization mean centroid $\langle M_{100}\rangle = \hat{M}_{100}$ is

$$\mu'_{200(\ell)}(t) \;=\; \int_{-\infty}^{\infty}\int_{-\infty}^{\infty}\int_{-\infty}^{\infty}\left(x-\hat{M}_{100}\right)^2 f_\ell(\vec{x},t)d\vec{x} \tag{12}$$

The realization mean of $\mu'_{200(\ell)}$ is

$$\langle\mu'_{200}\rangle \;=\; \frac{1}{N_r}\sum_{\ell=1}^{N_r}\mu'_{200(\ell)}(t) \tag{13}$$

From (9) one can establish that $\langle\mu'_{200}\rangle = \hat{\mu}_{200}$. The single-realization dispersivity is defined as $E_{xx(\ell)} = S'_{x\ell}/2$ where $S'_{x\ell}$ is the large-time slope of μ'_{200}. Thus the standard error of $\langle E_{xx}\rangle$ is approximated as $\hat{\sigma}_{E_{xx}}/\sqrt{N_r}$. In essence, this standard error is a reflection of our ability to accurately estimate the mean concentration field: as N_r becomes larger $\langle C(\vec{x},t)\rangle$ approximates $E[C(\vec{x},t)]$ more precisely, with the result that estimates $\langle E_{xx}\rangle$ of the mean dispersion coefficient $E[E_{xx}]$ also improve. The mean and standard error of E_{yy} and E_{zz} are similarly determined.

The dispersivity is defined as the dispersion coefficient normalized by the plume velocity; the longitudinal effective macrodispersivity A_{xx} is defined to be the mean macrodispersion coefficient divided by the mean plume velocity:

$$A_{xx} \;=\; \frac{\langle D_{xx}\rangle}{\langle V_c\rangle} \tag{14}$$

Transverse effective macrodispersivities A_{yy} and A_{zz} are similarly defined. To obtain an expression for the variance of this quantity, $\langle D_{xx} \rangle$ and $\langle V_c \rangle$ in (14) are replaced with perturbation expressions about their ensemble means, $\mu_{D_{xx}}$ and μ_{V_c}. Allowing $D'_{xx} = \langle D_{xx} \rangle - \mu_{D_{xx}}$ and $V'_c = \langle V_c \rangle - \mu_{V_c}$ to represent these perturbations, then

$$\frac{\langle D_{xx} \rangle}{\langle V_c \rangle} = \frac{D'_{xx} + \mu_{D_{xx}}}{V'_c + \mu_{V_c}} = \left(\frac{D'_{xx} + \mu_{D_{xx}}}{\mu_{V_c}} \right) \left[1 - \frac{V'_c}{\mu_{V_c}} + \left(\frac{V'_c}{\mu_{V_c}} \right)^2 - \cdots \right] \tag{15}$$

provided $V'_c / \mu_{V_c} < 1$ [*Gradshteyn and Ryzhik*, 1965, equation (1.112)]. Thus expressions for the first two non-central moments of A_{xx} become

$$E\left[\frac{\langle D_{xx} \rangle}{\langle V_c \rangle} \right] = \frac{\mu_{D_{xx}}}{\mu_{V_c}} \left(1 + \frac{\sigma^2_{\langle V_c \rangle}}{\mu^2_{V_c}} \right) - \frac{E[D'_{xx} V'_c]}{\mu^2_{V_c}} + \cdots$$

$$E\left[\frac{\langle D_{xx} \rangle}{\langle V_c \rangle} \right]^2 = \frac{\mu^2_{D_{xx}} + \sigma^2_{\langle D_{xx} \rangle}}{\mu^2_{V_c}} - 4 \frac{\mu_{D_{xx}} E[D'_{xx} V'_c]}{\mu^3_{V_c}} + 3 \frac{\mu^2_{D_{xx}} \sigma^2_{\langle V_c \rangle}}{\mu^4_{V_c}} + \cdots$$

As V'_c and D'_{xx} represent the deviation of the estimated mean from the ensemble mean, V'_c / μ_{V_c} and D'_{xx} / μ_{V_c} both should be small. A first-order expression for the variance of A_{xx} is obtained by subtracting the second expression from the square of the first and neglecting terms containing products of V'_c / μ_{V_c} and D'_{xx} / μ_{V_c} greater than two:

$$Var\left[A_{xx} \right] \approx \frac{\mu^2_{D_{xx}}}{\mu^2_{V_c}} \left[\frac{\sigma^2_{\langle D_{xx} \rangle}}{\mu^2_{D_{xx}}} - 2 \frac{E[D'_{xx} V'_c]}{\mu_{D_{xx}} \mu_{V_c}} + \frac{\sigma^2_{\langle V_c \rangle}}{\mu^2_{V_c}} \right] \tag{16}$$

The means $\mu_{D_{xx}}$ and μ_{V_c} can be estimated from the sample means, the variances $\sigma^2_{\langle D_{xx} \rangle}$ and $\sigma^2_{\langle V_c \rangle}$ are estimated as $\hat{\sigma}^2_{D_{xx}} / N_r$ and $\hat{\sigma}^2_{V_c} / N_r$ and the quantity $E[D'_{xx} V'_c]$ can be estimated from the sample cross correlation between D_{xx} and V_c: $\hat{\sigma}_{D_{xx} V_c} / N_r$. (The standard error for V_c is examined in the companion paper [*Naff et al.*, this issue].) Thus, the standard error for A_{xx} is approximated as

$$\hat{\sigma}_{A_{xx}} \approx \frac{\langle D_{xx} \rangle}{\langle V_c \rangle} \left[\frac{\hat{\sigma}^2_{D_{xx}}}{\langle D_{xx} \rangle^2} - 2 \frac{\hat{\sigma}_{D_{xx} V_c}}{\langle D_{xx} \rangle \langle V_c \rangle} + \frac{\hat{\sigma}^2_{V_c}}{\langle V_c \rangle^2} \right]^{1/2} \Big/ \sqrt{N_r} \tag{17}$$

One expects that statistics $\langle D_{xx} \rangle$ and $\langle V_c \rangle$ will not deviate greatly from their ensemble equivalents $\mu_{D_{xx}}$ and μ_{V_c}; thus, it is to be expected that (17) will be a good estimator of the standard error of A_{xx}. Error bars for macrodispersivities A_{xx}, A_{yy} and A_{zz} appearing in the following figures are based on (17) or its equivalent. The error bars for macrodispersivities A'_{xx}, A'_{yy} and A'_{zz} for the mean cloud are similarly derived.

Before proceeding to the next section, we note that one of the first tests of these simulations was to verify that that the mean macrodispersion coefficients $\langle D_{xx} \rangle$, $\langle D_{yy} \rangle$, $\langle D_{zz} \rangle$ and $\langle E_{xx} \rangle$, $\langle E_{yy} \rangle$, $\langle E_{zz} \rangle$ form a linear relationship with the mean centroidal velocity $\langle V_c \rangle$. This was accomplished by changing the simulated gradient across the flow cell while holding all other parameters constant. The mean macrodispersivities and mean centroid velocities were estimated for each gradient scenario; 19 realization MC simulations were used throughout this test. The mean macrodispersivities were plotted against their corresponding velocities, and straight lines fit to the resulting plots. The results strongly indicate that the mean macrodispersion coefficients form a linear relation with the mean centroidal velocity.

Macrodispersivities and Variation in Hydraulic Conductivity Field

In this section, the effect of variation in the hydraulic conductivity field on macrodispersion of the tracer cloud is examined. In the process, three different measures of the macrodispersivity, as pertaining to the mean cloud and individual cloud realizations, are considered. In this modelling scenario $\hat{\sigma}_f^2$ was allowed to vary from MC simulation to MC simulation, but the medium correlation length scales were held constant such that $\hat{\lambda}_x = 2.77\ m$, $\hat{\lambda}_y = 2.79\ m$ and $\hat{\lambda}_z = 0.278\ m$; thus, $\hat{\lambda}_h/\hat{\lambda}_z$ is approximately 10. The vertical dimension of the initial source box is $0.5\ m$; local longitudinal and transverse dispersivities α_ℓ and α_t are $0.1\ m$ and $0.01\ m$ respectively. These 20 realization MC simulations correspond to the first scenario in Table 1. It should be noted that the minimum plume-centroid travel distance for each of the 20 realization simulations decreased as $\hat{\sigma}_f^2$ increased; for $\hat{\sigma}_f^2 = 0.087$, $\sim 12\hat{\lambda}_x$ were traversed, while for $\hat{\sigma}_f^2 = 0.874$, $\sim 8\hat{\lambda}_x$ were traversed. The second-moment information associated with the largest variance appears not unlike that for $\hat{\sigma}_f^2 = 0.349$ depicted in Figure 4. Thus, although the late time portion of the second moment curves used to derive the macrodispersivities is smaller for the case where $\hat{\sigma}_f^2 = 0.874$, we do not believe that the resulting macrodispersivity estimates were excessively degraded.

Figure 3 depicts the the effective macrodispersivities $A_{xx} = \langle D_{xx}\rangle/\langle V_c\rangle$, $A_{yy} = \langle D_{yy}\rangle/\langle V_c\rangle$ and $A_{zz} = \langle D_{zz}\rangle/\langle V_c\rangle$, for the individual realizations, and mean-cloud macrodispersivities $A'_{xx} = \langle E_{xx}\rangle/\langle V_c\rangle$, $A'_{yy} = \langle E_{yy}\rangle/\langle V_c\rangle$ and $A'_{zz} = \langle E_{zz}\rangle/\langle V_c\rangle$. The x-direction macrodispersivities, A_{xx} and A'_{xx}, exhibit the relation $A'_{xx} > A_{xx}$ (Figure 3c); the difference between these quantities represents dispersion of individual plume centroids about the ensemble mean plume centroid. Linear curves fit to both A'_{xx} and A_{xx} indicate that their intercepts are approximately equal to the input local longitudinal dispersivity, α_ℓ; excluding intercepts, the effective macrodispersivity, $A_{xx} = \langle D_{xx}\rangle/\langle V_c\rangle$, is about half the mean-cloud dispersivity A'_{xx}.

The mean-cloud macrodispersivity, A'_{xx}, has the approximate linear relation

$$(A'_{xx} - \alpha_\ell) \;=\; 0.72\hat{\sigma}_f^2\hat{\lambda}_x$$

The MC results for A'_{xx} do have a slight tendency to depart from a linear relation with $\hat{\sigma}_f^2$ as $\hat{\sigma}_f^2$ increases; this tendency is illustrated with the fit line in Figure 4. One cannot say, with this data set, that this tendency is significant; we intrepret these results as favoring a linear or near-linear relation with $\hat{\sigma}_f^2$.

A number of analytical results, based on the stochastic partial differential equations governing flow and transport phenomena, are available for the mean-cloud longitudinal macrodispersivity A'_{xx}; these enable one to estimate A'_{xx} on theoretical grounds. First-order analyses for A'_{xx} that exclude the effect of local dispersion suggest that [*Dagan*, 1984]

$$(A'_{xx} - \alpha_\ell) = \sigma_f^2\lambda_x \tag{18}$$

or [*Gelhar and Axness*, 1983]

$$(A'_{xx} - \alpha_\ell) = \sigma_f^2\lambda_x/\gamma^2 \tag{19}$$

where $\gamma = 1+\beta\sigma_f^2$ is the flow factor. For the flow scenarios presented by the MC simulations in this paper, $\beta = 1/2 - g_{11}$, where g_{11} is defined by equation (9) of the companion paper [*Naff et al.*, this issue]; estimated parameters for this scenario indicate that $\beta \approx 0.43$. The first of these results, without the flow factor γ, overestimates A'_{xx} of Figure 3c by a factor of 1.4 (Figure 4). Inclusion of the flow factor gives fair agreement with the MC simulations up to $\sigma_f^2 = 0.4$; however, for larger values of σ_f^2, the agreement degrades badly. A second-order result by *Naff* [1994, equation (45*b*)], again for negligible local dispersion, suggests that the longitudinal mean-cloud macrodispersivity should be

$$(A'_{xx} - \alpha_\ell) \;=\; \sigma_f^2\lambda_x\left(1 - \frac{\sigma_f^2}{4}\right) \tag{20}$$

Given the above parameter estimates, this result produces values of A'_{xx} which overestimate the MC results by a factor of about 1.2 (Figure 4); additionally, the coefficient for the second-order correction term, σ_f^4, imparts more curvature to A'_{xx} than suggested by the MC results. While this second-order approximation does appear to be an improvement over the first-order approximations (18) or (19), a variant of a first-order result presented by *Gelhar and Axness* [1983], which considers local dispersion in its formulation, appears to give a superior fit to the MC results for small values of σ_f^2.

The effect of local dispersion on the x-direction macrodispersion can be evaluated from a result given by *Gelhar and Axness* [1983]; their first-order approximation for A'_{xx} indicates that

$$(A'_{xx} - \alpha_\ell) \;=\; \frac{I(r)}{\gamma^2}\sigma_f^2\lambda_x \tag{21}$$

where $\gamma = 1 + \beta\sigma_f^2$ is the same flow factor as in (19), $I(r)$ is the integral

$$I(r) \;=\; \int\int\int_{-\infty}^{\infty} \frac{r z^2 \; dx\, dy\, dz}{(r^2 z^4 + x^2)(1 + x^2 + y^2 + z^2)^2}$$

and $r = \alpha_t/\lambda_z \cdot \lambda_x/\lambda_z$. For values of r such that $0 \le r < 2.5$, $I(r)$ is closely approximated by the following expression:

$$I(r) \;=\; 1 - r + ar(1 - e^{-br^c})$$

where $a = 0.9014$, $b = 1.3854$ and $c = 0.557$; this expression was obtained by fitting after integrating $I(r)$ numerically. Note that the function $I(r)$ responds to both changes in the statistical anisotropy λ_x/λ_z and normalized local transverse dispersivity α_t/λ_z; the relation is approximate in that it assumes that local dispersion, except in the dimensionless form r can be ignored and that the statistical anisotropy is large. When $\beta\sigma_f^2 < 1$, the effect of the flow factor on (21) can be appreciated from the approximation $\gamma^{-2} \approx 1 - 2\beta\sigma_f^2$; thus, the flow factor has the effect of introducing a significant higher-order term, of the magnitude σ_f^4,

in (21). The MC results for A'_{xx} do not indicate that the inclusion of higher-order terms of this nature is warranted; that is, curve A'_{xx} of Figure 3c is very nearly linear in σ_f^2. *Dagan* [1988] indicates that inclusion of the flow factor results from an inconsistent expansion by *Gelhar and Axness* [1983], which suggests that it should be removed from their results; if one drops γ from (21), then

$$(A'_{xx} - \alpha_\ell) \;=\; I(r)\sigma_f^2 \lambda_x \tag{22}$$

results. Parameter estimates given previously indicate that $r \approx 0.36$; with the flow factor set to unity to eliminate the presence of a higher-order term, then (22) overestimates A'_{xx} from the MC simulations by a factor of 1.1 (Figure 4). If the flow factor γ is included, as indicated in (21), then good agreement is achieved up to a σ_f^2 of 0.2, after which it underestimates the MC simulations by an amount which increases significantly with increasing σ_f^2. Comparison of these first-order approximate results with the MC simulations suggests that the inclusion of a flow factor in the first-order analyses of *Gelhar and Axness* [1983] and *Naff* [1990] overcompensates by decreasing A'_{xx} excessively as σ_f^2 increases. For an analytical approximation to give good agreement over the entire range depicted in Figure 3, it is likely that a second-order approximation which incorporates the effects of local dispersion will be necessary. One can conjecture that such a relation would have the form of both (20) and (22); that is

$$(A'_{xx} - \alpha_\ell) \;=\; \sigma_f^2 \lambda_x I(r) \left(1 - \frac{\sigma_f^2}{4}\right) \tag{23}$$

This conjecture gives the best fit of any of the equations (Figure 4), but still deviates significantly from the MC results for large values of σ_f^2.

Figures 3a and 3b are depictions of the transverse macrodispersivities for the above flow scenario. Again, the intercept of the fit lines is nearly equal to the input local transverse dispersivity α_t and $A'_{yy} \geq A_{yy}$, $A'_{zz} \geq A_{zz}$. Before discussing these estimates of the transverse macrodispersivities in detail, examples of the second moments in the y and z directions are examined so as to better understand the origin of these results. Figure 5 depicts the x, y and z direction second moments for the simulation where $\hat{\sigma}_f^2 = 0.349$. The contribution of local dispersion to the overall second moment, approximated by either $2\alpha_\ell \langle V_c \rangle t$ (longitudinal) or $2\alpha_t \langle V_c \rangle t$ (transverse), is indicated by the dotted lines on this figure. The transverse mean-cloud variances, $\hat{\mu}_{020}$ and $\hat{\mu}_{002}$, and mean-realization variances, $\langle \mu_{020} \rangle$ and $\langle \mu_{002} \rangle$, increase uniformly with dimensionless time for the ten length scales where all 20 realizations are represented (Figures 5a and 5b). Most analytical results suggest that this should not be the case [e.g., *Dagan*, 1994]; that, at least for $\hat{\mu}_{020}$ and $\hat{\mu}_{002}$, these curves should change slope and, in large time, approximately parallel the variance contribution of local transverse dispersion, $2\alpha_t \langle V_c \rangle t$. These MC results suggest that these measures of transverse cloud variance increase linearly with time but at a rate faster than can be explained by local dispersion. As a result, we have elected to use straight-line fits to late-time second-moment data to estimate transverse macrodispersivities in both the y and z directions; the result is the depictions of the transverse macrodispersivity seen in Figures 3a and 3b.

There are very few theoretical results available which mimic, in some sense, either the transverse second moments or transverse macrodispersivity MC results. The analysis by *Zhang and Neuman* [1990] does indicate that, in late time, the second moments $\hat{\mu}_{020}$ and $\hat{\mu}_{002}$ should increase linearly at a rate faster than $2\alpha_t \langle V_c \rangle$. Their development requires the evaluation of the Peclet number $P = \lambda_x / A'_{xx}$, which for the results in this section varies from about 1.5 for the largest value of $\hat{\sigma}_f^2$ to 10 for the smallest. Their analysis indicates that values for the theoretical transverse macrodispersivities can be obtained as

$A'_{yy} - \alpha_t = \beta_{yy}(P)\sigma_f^2\lambda_x$ and $A'_{zz} - \alpha_t = \beta_{zz}(P)\sigma_f^2\lambda_x$ where values for the dimensionless coefficients β_{yy} and β_{zz} can be crudely estimated from their Figures 2 and 3 respectively. Their Figure 2 indicates that, for the above range of Peclet numbers, β_{yy} varies between 0.0009 when $\hat{\sigma}_f^2 = 0.0874$ to 0.004 when $\hat{\sigma}_f^2 = 0.874$; thus their theoretical result for $A'_{yy} - \alpha_t$ suggest that this quantity should vary between about 0.0002 m and 0.01 m. The quantity $A'_{yy} - \alpha_t$ of Figure 3a actually varies between 0.009 m and 0.011 m, which shows agreement with these theoretical results for the larger values of $\hat{\sigma}_f^2$. Similarly, β_{zz} varies between about 0.003 when $\hat{\sigma}_f^2 = 0.0874$ to about 0.009 when $\hat{\sigma}_f^2 = 0.874$; thus the theoretical value of $A'_{zz} - \alpha_t$ should vary between about 0.0007 m and 0.02 m. The quantity $A'_{zz} - \alpha_t$ of Figure 3b actually varies between 0.002 m and 0.026 m, which also suggests, for large σ_f^2, that some agreement between theoretical and MC analyses may exist. It is doubtful, in both cases, that the analysis of *Zhang and Neuman* [1990] could agree over the full range of values for $\hat{\sigma}_f^2$ demonstrated in Figure 3 as the iterative procedure they use to implement Corrsin's conjecture most likely introduces a fairly strong nonlinearity with respect to σ_f^2; this may also explain the large deviation from the MC results for small values of $\hat{\sigma}_f^2$. The macrodispersivities A'_{yy} and A'_{zz} of Figure 3 do demonstrate some nonlinearity with respect to $\hat{\sigma}_f^2$, but the nature of the nonlinearity is such that they are opposite each other; an explanation for this nonlinearity in the MC results is not readily available.

Before leaving this section, we briefly examine another measure of the effective macrodispersivity. Using the same time intervals as used to derive A_{xx}, A_{yy} and A_{zz}, one can estimate the macrodispersivities $A''_{xx(\ell)} = D_{xx(\ell)}/V_{c(\ell)}$, $A''_{yy(\ell)} = D_{yy(\ell)}/V_{c(\ell)}$ and $A''_{zz(\ell)} = D_{zz(\ell)}/V_{c(\ell)}$ for individual cloud realizations. The mean of these realization dispersivities, $\langle A''_{xx} \rangle$, $\langle A''_{yy} \rangle$ and $\langle A''_{zz} \rangle$, is the expectation of what the dispersivity might be for any single experiment; as such, it is more representative of the parameter that would be applied in a field situation. These mean macrodispersivities, depicted in Figure 6, are very similar to the effective dispersivities A_{xx}, A_{yy} and A_{zz}, generally being only very slightly greater. (Dashed

lines on this figure are the fit lines for A_{xx}, A_{yy} and A_{zz} of Figure 3.) This difference, however, increases as $\hat{\sigma}_f^2$ increases; for heterogeneous formations where $\sigma_f^2 > 1$, one might expect that the difference between these two measures of macrodispersivity to be significant. When $\sigma_f^2 < 1$, it appears that the effective macrodispersivities, defined from a ratio of means, are good measure of the mean macrodispersivities.

Length Scales and Statistical Anisotropy

Since a relatively small number of realizations constitute each MC simulation, and as variability in the simulations decrease as a function of $1/\sqrt{N_r}$, where N_r is the number of realizations in a MC simulation, some variability from this source is present in all results presented in this paper. When it can be arranged that the same set of random-field realizations for a MC scenario be used for every simulation, as done in the previous section, then at least the overall trend from this scenario should not be obscured by this source of variability. The manner in which the random field generator was implemented in the code does not allow for one easily to change length scales from one MC simulation to the next and yet use the same set of randomly generated hydraulic conductivities for every simulation. As a consequence, a different set of random field realizations for each length-scale scenario was used in obtaining the principal results of this section. The major consequence of this procedure is that it is more difficult to discern trends in the resulting macrodispersivity data as there is sufficient variation between 20 realization MC simulation results that, in some cases, any significant trends are obscured. This difficulty is used in this section as an opportunity to examine the intrasimulation variability that one might expect from a typical 20 realization MC run.

The principal objective of this section is to obtain insight of the effect of statistical anisotropy on the various measures of macrodispersion. To this end four MC simulations (scenario 2, Table 1) were run where the effective length scales in the horizontal plane, $\hat{\lambda}_x$, was varied from 1.42 m to 5.50 m; again $\hat{\lambda}_y \approx \hat{\lambda}_x$. The z-direction scale $\hat{\lambda}_z$ also varies, but within the narrow range of 0.270 m to 0.284 m; the anisotropy ratio, $\hat{\lambda}_x/\hat{\lambda}_z$, varies from about 5 to 20. The variance in log hydraulic conductivities, $\hat{\sigma}_f^2$, similarly varies in the narrow range of 0.517 to 0.528. To accommodate this variation in $\hat{\lambda}_x$ in the transport simulations, the domain size was varied as $\hat{\lambda}_x$ varied. For $\hat{\lambda}_x = 1.42$ m, the $x \times y \times z$ dimensions of

the domain were $43 \times 10 \times 15\ m^3$; this increased to $90 \times 11 \times 18\ m^3$ for $\hat{\lambda}_x = 5.50\ m$. It should be noted that, in terms of length scales $\hat{\lambda}_x$, the domain for $\hat{\lambda}_x = 1.42\ m$ is about twice that of $\hat{\lambda}_x = 5.50\ m$ in the x direction; given the numerical exigencies of the transport simulations, this was about the maximum relative size that could be afforded the $\hat{\lambda}_x = 5.50\ m$ simulation. Each 20 realization MC simulation was repeated with a second 20 realization simulation using a different, independent set of hydraulic conductivities. Even with the aforementioned enlargement in domain size for the $\hat{\lambda}_x = 5.50\ m$ simulation, the maximum travel distance of the plume before a boundary encounter by a plume realization was $\sim 5.5\hat{\lambda}_x$. This is a significantly shorter relative travel distance than the ten lenght scales usually obtained in these MC simulations; this shorter relative travel may have contributed to the rather poor results for this simulation and also, to a lesser extent, to the MC simulation corresponding to $\hat{\lambda}_x = 4.14\ m$ $\left(t\langle V_c\rangle/\hat{\lambda}_x|_{max} \approx 7\right)$.

The basic results of these simulations are presented in Figure 7. An obvious point of this figure is that the macrodispersivities from the mean cloud are rather more poorly determined than the effective macrodispersivities; even though individual datum, as judged by the error bars, may be relatively well determined, the intersimulation variability, as determined by comparing repeat simulations, can be quite large. This greater variability, for the mean-cloud macrodispersivities, probably results from uncertainty in the location of the plume centroid; this source of variability is not present in the effective macrodispersivity estimates. For the transverse components, A'_{yy} and A'_{zz}, the large variability in the mean-cloud macrodispersivity estimates eliminates any possibility of determining a trend (other than the mean) in this data; the slopes for the fit lines for these transverse components depicted in in Figure 7 are not statistically significant. The slopes for the effective transverse macrodispersivites, A_{yy} and A_{zz}, are significant and indicate that the effective transverse macrodispersivities decrease ever so slightly with increasing $\hat{\lambda}_x$ or statistical anisotropy.

The x-direction macrodispersivities, both mean-cloud and effective, indicate a distinctive trend with increasing $\hat{\lambda}_x$ (Figure 7c); however, the rate of increase in A_{xx} and A'_{xx} with increasing $\hat{\lambda}_x$ is more subdued then one might expect. This effect is better illustrated by plotting $A_{xx}/\hat{\lambda}_x$ and $A'_{xx}/\hat{\lambda}_x$ against $\hat{\lambda}_x/\hat{\lambda}_z$, as depicted in Figure 8. Here it is evident that these normalized quantities actually decrease with increasing statistical anisotropy $\hat{\lambda}_x/\hat{\lambda}_z$; this decrease has the appearance of asymptotically becoming constant as $\hat{\lambda}_x/\hat{\lambda}_z$ increases. One may question whether, given the variability in the data, this apparent decrease in $A_{xx}/\hat{\lambda}_x$ and $A'_{xx}/\hat{\lambda}_x$ with increasing statistical anisotropy isn't happenstance. To act as a check against this possibility, a second set of 20 realization runs were carried out where the statistical anisotropy was created by shrinking or enlarging the flow cell in the z direction; thus, $\hat{\lambda}_x$ was held constant at 3.28 m and $\hat{\lambda}_z$ was allowed to vary from 0.165 m to 0.496 m. However, if relation (22) is to be believed, then one must hold the ratio $\hat{\lambda}_z/\alpha_t$ constant when attempting to investigate the effect of physical anisotropy by varying $\hat{\lambda}_z$ in this manner. In any case, it was necessary to hold this ratio constant to ensure stability of the numerical solution and to maintain the plume within the lateral domain boundary. Thus, these simulations were run with $\hat{\lambda}_z/\alpha_t = 27.5$, which required that α_t be varied as $\hat{\lambda}_z$ increased or decreased. For this test, $\hat{\sigma}_f^2$ was held constant at 0.443 (scenario 3, Table 1). This procedure allowed the use of the same set of random fields for every length-scale scenario, avoiding the variability resulting from changing random-field sets. These x-direction macrodispersivity results, depicted in Figure 9, are not unlike those for Figure 8, indicating that the decrease in $A_{xx}/\hat{\lambda}_x$ and $A'_{xx}/\hat{\lambda}_x$ with increasing statistical anisotropy is not simply happenstance and that the use of the dimensionless parameter $r = \alpha_t/\lambda_z \cdot \lambda_x/\lambda_z$ in equation (22) to approximate the effect of transverse local dispersion on the macrodispersive process is not without merit.

The above results suggest that an interaction of the local lateral mass tranfer and large-scale anisotropy is affecting the longitudinal macrodispersive process; the function $I(r)$ of (21), with its dependence on the dimensionless parameter $r = \alpha_t/\lambda_z \cdot \lambda_x/\lambda_z$, may be useful to explain this effect. To investigate further the extent to which the factor $I(r)$ can explain the observed decrease in $A'_{xx}/\hat{\lambda}_x$ in these MC simulations, a slightly modified form of the conjectured equation (23) is used. As noted in the previous section, (23) with its second-order approximation in σ_f^2 and first-order approximation for local dispersion, is a fair model of mean-cloud longitudinal macrodispersivity A'_{xx} when σ_f^2 is allowed to vary (scenario 1). Noting that, to second order,

$$2\left(1 - e^{-\sigma_f^2/2}\right) \approx \sigma_f^2\left(1 - \frac{\sigma_f^2}{4}\right)$$

then an extension of the previous conjecture suggests that

$$A'_{xx} - \alpha_\ell = 2\left(1 - e^{-\sigma_f^2/2}\right)\lambda_x I(r) \tag{24}$$

where $I(r)$ is identical to that given in (21). Normalized estimates of A'_{xx} for these two MC scenarios have been plotted in Figure 10; local longitudinal dispersion α_ℓ was subtracted from the estimates of A'_{xx} to make these results compatible with (24). The use of $2\left[1 - exp(-\sigma_f^2/2)\right]$ in place of $\sigma_f^2\left[1 - (\sigma_f^2/4)\right]$ to normalize $A'_{xx} - \alpha_\ell$ has only a very minor effect on the plotted values (this statement is also true of Figure 4, equation (23)). In this plot, the normalized MC macrodispersivity data tend to fall below the $I(r)$ curve, with a very few points actually falling on the curve. This result may reflect some difficulty in obtaining, with these limited MC simulations, good estimates of the second moment $\hat{\mu}_{200}$; it may be inherently easier to underestimate $\hat{\mu}_{200}$ then to overestimate this quantity. Also, there remains the fact that $I(r)$ gives only an approximate correction for the effect of statistical anisotropy; the approximation should improve as λ_x/λ_z increases, although this behavior is not apparent from Figure 10. While the the fit of the $I(r)$ curve to these MC results is far

from perfect, it does suggest that $I(r)$ at least partially accounts for the observed trend in the A'_{xx} data.

Effect of Local Transverse Dispersivity

First-order analyses indicate that the local transverse dispersivity, α_t, can have a pronounced effect on the global dispersion process [*Gelhar and Axness*, 1983; *Naff*, 1990; *Zhang and Neuman*, 1990]. In this study, the effect of local dispersion on the macrodispersivities is examined with MC simulations in which values of α_t was allowed to range over an order of magnitude ($0.05\ m$ to $0.5\ m$) and α_ℓ was held constant at $0.1\ m$ (scenario 4, Table 1). These simulations were constructed with constant length scales ($\hat{\lambda}_x = 2.78\ m$, $\hat{\lambda}_y = 2.79\ m$ and $\hat{\lambda}_z = 0.278\ m$) and variance in hydraulic conductivity ($\hat{\sigma}_f^2 = 0.527$). As the same set of hydraulic-conductivity realizations were used for all α_t values of the MC scenario, it was necessary to initially size the domain for the largest local transverse dispersivity used in these simulations ($\alpha_t = 0.5\ m$). That is, the domain had to be large enough that local lateral dispersion would not cause excessive contact between the lateral edge of the cloud and the domain boundary. However, to obtain a stable solution when modelling with smaller dispersivity values it also was necessary to include extra nodes in the lateral direction. To provide an adequate resolution of the tracer cloud when α_t was at the scenario minimum ($0.05\ m$) required a discretization with $\sim 1.2 \times 10^6$ nodes.

Second-moment curves for the MC simulation where $\alpha_t = 0.01\ m$ are depicted in Figure 11; note that the mean longitudinal curve $\langle \mu_{200} \rangle$ is convex downward in late time, while the transverse curves $\langle \mu_{020} \rangle$ and, to a lesser degree, $\langle \mu_{002} \rangle$ are convex upward. A possible explanation for this phenomena is that the tracer fluid encountered a predominance of low conductivity zones downgradient of the source box, causing the clouds, on average, to bulge laterally in the process of passing these zones. From the first moment curves in the x direction it is difficult to detect a significant slowing of the mean plume for this scenario, as might be expected from the proposed explanation. However, the first moment curves in the y and z directions (not shown in this paper) indicate that the mean plume does deviate slightly from a path consistent with the center of the upstream and downstream faces

of the flow cell; this deviation continues for a travel time of about 200 days, after which the plume centroid tends back toward the centerline of the flow cell. The transverse velocity component created by this deviation is, at a maximum, about two orders of magnitude less than the mean plume velocity in the x direction ($0.001m/d$ versus $0.1m/d$). The existence and severity of bows in second-moment curves, as noted previously, is dependent on the particular set of hydraulic-conductivity fields used in MC simulations resulting in these curves. If the upward convexity of the $\langle\mu_{020}\rangle$ and $\langle\mu_{002}\rangle$ curves results from a tendency for the realization to realization hydraulic conductivity downgradient of the source box to be slightly smaller than the domain average, then downward convexity should indicate an opposite effect; that there exists a tendency for the clouds to be channelled through zones of slightly higher conductivity.

As discussed earlier, these bows create a problem in that it is difficult to discern when the late-time asymptotic aspect of the cloud development has begun. For this MC scenario and consistent with our concept of asymptotic behavior for these second moments, we chose to use only the last few points on each mean second-moment curve as a basis for the macrodispersivity estimates. Use of segments corresponding to these points is based in the belief that development of asymptotic linear behavior, characteristic of late-time mean second-moment curves, was delayed. This concept of delayed development is reinforced by the behavior of the coefficient of skewness curves, which will be presented subsequently. If one ignores the bows evident in Figure 11 when deriving the macrodispersivities and uses most of the late-time data, then decidedly different macrodispersivity estimates emerge. An additional complication which results from using only the very latest time data for the determination of macrodispersivities is that, for the scenario where $\alpha_t = 0.05\ m$, one plume realization encountered the detection boundary at 275 days ($t\langle V_c\rangle/\hat{\lambda}_x \approx 10$); thus, the full 20 realization set is available for times up to, but not including, 275 days. As it is desirable to retain the last two data points for all α_t scenarios, the offending realization was

removed and 19 realizations were used for the following analysis. Thus, macrodispersivity estimates depicted in this section are not only based on the very latest second-moment data, but also on 19, rather than 20, realizations. The amount and lateness of bowing depicted in Figure 11 is, in our experience, unusual for 20 realization MC simulations used in this study. Some variability from simulation to simulation, because of the small number of realizations used, is to be expected, but usually little problem was encountered in selecting an interval appropriate for the estimation of the macrodispersivities.

Macrodispersivity estimates resulting from using the very late time portion of each curve are depicted in Figure 12. The x-direction macrodispersivities, A_{xx} and A'_{xx} decrease as α_t increases (Figure 12c); the behavior of this decrease is similar to that for statistical anisotropy, as discussed in the previous section. The transverse vertical macrodispersivities, A_{zz} and A'_{zz}, are initially larger than the local transverse dispersivity α_t by a factor of about two. However, as α_t increases this difference dissipates and, when $\alpha_t = 0.05\ m$, A_{zz} is essentially equal to α_t (Figure 12b). For the effective transverse vertical macrodispersivity A_{zz}, it would appear that, by increasing α_t, one can swamp out whatever effect medium heterogeneity has on the lateral macrodispersion process. The difference between the mean-cloud macrodispersivity, A'_{zz}, and the effective macrodispersivity, A_{zz}, remains constant or increases slightly with increasing α_t; this result suggests that variation in plume centroid in the z direction remains a factor, even though A_{zz} becomes essentially identical to α_t. The transverse horizontal macrodispersivities, A_{yy} and A'_{yy}, are essentially identical and equal to α_t for all values of α_t (Figure 12a). This latter result is contrary to scenario 1, where it was found that $A'_{yy} > A_{yy} > \alpha_t$(Figure 3a).

In Figure 13, the mean-cloud longitudinal macrodispersivity estimates, A'_{xx}, have been normalized and plotted as a function of $r = \alpha_t/\lambda_z \cdot \lambda_x/\lambda_z$; equation (24) was used for normalization. Also plotted on this figure is the function $I(r)$ from (21). Except at smaller values of r, the estimated macrodispersivities largely exceed the function $I(r)$; indeed, this result suggests that, as α_t (and therefore r) increases, there exists a limit as to the amount of decrease to be expected in A'_{xx} (in general, $I(r)$ tends to zero as r increases). As the correction factor $I(r)$ is only an approximation for the effect of α_t on A'_{xx} and as that approximation assumes that α_t is small, it is perhaps not surprising that the fit degrades with increasing α_t. While the results of this and the previous section indicate that the use of the function $I(r)$ to describe the functional relation of A'_{xx} with the physical anisotropy λ_x/λ_z and local transverse dispersivity α_t may not be precise, doing so captures at least the first-order effect of these variables on the mean-cloud longitudinal dispersivity.

Ergodicity: Effect of Source Size and Local Transverse Dispersivity

In this paper ergodic behavior implies that, as the tracer cloud from a single realization grows to encompass multiple length scales of the medium, the moments of this single realization cloud will mimic the ensemble moments. To observe whether ergodicity is applicable, in this sense, one would ideally have a very large domain over which one could observe cloud development for a very large time; although evidence along these lines is presented, computational exigencies do not permit a complete simulation. In this section, two parameters which are believed to have a similar effect are examined: these are the source size I_z in the vertical direction and the local transverse dispersivity α_t. To measure whether altering these parameters has any effect on the ergodic behavior of the cloud, we observe the variance in two x-direction moments: the centroid M_{100} and the second central moment μ_{200}. Because the means and variances in both of these moments grow with travel time, it is important to use relative measures of variability when determining whether the process is ergodic. For the relative variability in $M_{100}(t)$, a pseudodispersivity $\Gamma_{xx}(t)$ can be defined such that

$$\Gamma_{xx}(t) = \frac{1}{2\langle V_c \rangle} \frac{d}{dt} S_{200}(t) \tag{25}$$

where $S_{200}(t)$ is the variance in the x centroid as defined in (11b). In reference to equation (10), then

$$A'_{xx}(t) = A_{xx}(t) + \Gamma_{xx}(t) \tag{26}$$

That is, the difference between the mean-cloud macrodispersivity A'_{xx} and the effective macrodispersivity A_{xx} is the pseudodispersivity Γ_{xx}. An estimate for $dS_{200}(t)/dt$ can be determined from the late-time portion of the variance curve, where the slope is essentially constant. However, using the late-time portion of the curve to estimate the slope is not always desirable. For scenario 1 in particular the maximum slope of the $S_{200}(t)$ curves will be used for reasons which will be clarified later. For most $S_{200}(t)$ curves examined in this

study, the maximum slope corresponds to the late-time slope. If, for some scenario, Γ_{xx} were found to be small, then the mean-cloud and effective macrodispersivities would be essentially identical. With regard to the variance in the second moment μ_{200}, the coefficient of variation shall be used as the relative measure of variability:

$$C_v[\mu_{200}(t)] \;=\; \frac{\sqrt{\langle(\mu_{200}(t) - \langle\mu_{200}(t)\rangle)^2\rangle}}{\langle\mu_{200}(t)\rangle} \tag{27}$$

Using the coefficient of variation to report the variation in μ_{200} has the advantage of allowing one to determine the size of this variation relative to the mean; if $\langle\mu_{200}\rangle$ is much larger than $\sqrt{\langle(\mu_{200}(t) - \langle\mu_{200}(t)\rangle)^2\rangle}$ then, relative to the mean, the variation in the second moment is of little consequence. This relative measure of variability is particularly important for variables such as μ_{200} which have means that vary as functions of time as well as their parameters. The importance of this concept is perhaps best illustrated by defining a new random variable χ such that $\chi = \mu_{200}/\langle\mu_{200}\rangle$; this normalized variable has a constant mean (unity) and its variance is $C_v^2[\mu_{200}]$. A behavior whereby $C_v[\mu_{200}]$ tends to zero implies that χ is tightly distributed about its mean and therefore $\mu_{200} \rightarrow \langle\mu_{200}\rangle$ in probability.

The effect of source size is investigated for the case where $\hat{\lambda}_x = 2.78\ m$, $\hat{\lambda}_y = 2.79\ m$ and $\hat{\lambda}_z = 0.278\ m$; the estimated variance in log hydraulic conductivity, $\hat{\sigma}_f^2$, is 0.512 (scenario 5, Table 1). Local dispersivities are $\alpha_\ell = 0.1\ m$ and $\alpha_t = 0.01\ m$. Figure 14 illustrates the effect of source size I_z on Γ_{xx}; clearly Γ_{xx} decreases (albeit slowly) as the ratio $I_z/\hat{\lambda}_z$ increases. Qualitatively, this result agrees with that predicted by *Dagan* [1990, 1991]. Because $\langle M_{100}\rangle$ is essentially identical for all ratios shown, this result also indicates that the variance in M_{100} is itself decreasing as the ratio $I_z/\hat{\lambda}_z$ increases. Extrapolation of the curve fit through these data suggest that, when $I_z \approx 12\lambda_z$, Γ_{xx} would be essentially null; while this extrapolation is hazardous, it should be indicative of the minimum source size I_z, for transport in three-dimensional heterogeneous porous media, required in order for A'_{xx} and A_{xx} to be approximately equal. Unfortunately, the effect of source size I_z on $C_v[\mu_{200}]$ is indicative of

nonergodic behavior; that is, as $I_z/\hat{\lambda}_z$ increases, so does $C_v[\mu_{200}]$. This result is depicted in Figure (15), where $C_v[\mu_{200}]$ has been plotted against dimensionless travel time (a curve for the case where $I_z/\hat{\lambda}_z = 0.45$ is not included on this figure for clarity; it is very similar to the curve for $I_z/\hat{\lambda}_z = 0.91$). This increase in $C_v[\mu_{200}]$ occurs in spite of the fact that $\langle\mu_{200}\rangle$ increases with increasing $I_z/\hat{\lambda}_z$; thus, not only is the standard deviation in μ_{200} increasing as a function of $I_z/\hat{\lambda}_z$, it is doing so at a faster rate than the increase in the mean. This result is counter intuitive, as one would assume that larger spatial averages would tend to reduce variability in the second central moment. While this evidence isn't conclusive, it does indicate that the attainment of a quasi-ergodic state by increasing the source size is more complicated than indicated by *Dagan* [1991].

The effect of local dispersion on ergodicity is investigated in scenario 4 (Table 1) where $\hat{\lambda}_x = 2.78\ m$, $\hat{\lambda}_y = 2.79\ m$ and $\hat{\lambda}_z = 0.278\ m$; the estimated variance in log hydraulic conductivity, $\hat{\sigma}_f^2$, is 0.527. Transport parameters consist of $\alpha_\ell = 0.1\ m$ and $I_z = 1.8\hat{\lambda}_z$. As explained previously, these results are based on simulations consisting of 19 MC realizations. Figure 16 illustrates the effect of varying α_t on Γ_{xx}. Clearly, increasing α_t can reduce Γ_{xx} significantly; however, the rate of reduction decreases as α_t increases. Qualitatively, this result agrees with that of *Rajaram and Gelhar* [1993]. If one hazards to extrapolate the fit line in this figure, then when $\alpha_t \approx 0.64\lambda_z$ the pseudodispersivity Γ_{xx} should be null; it is unseeming that α_t could obtain such values in natural aquifers. Increasing α_t also has the effect of reducing $C_v[\mu_{200}]$ (Figure 17); the difference is particularly pronounced in late time. These results suggest that the normalized variable $\mu_{200}/\langle\mu_{200}\rangle$ tends to unity as α_t increases. Increasing lateral mixing appears to be more effective than increasing source size as a means of achieving a quasi-ergodic state; this result probably reflects the additional smoothing imparted to any single cloud by the enhanced transverse dispersion. While these results are indicative of the smoothing effect that can be imparted by local transverse dispersion,

it must be realized that α_t and the hydraulic conductivity $K(\vec{x})$ fields are most likely correlated; in a natural aquifer, a change in α_t would be most likely accompanied by a corresponding change in $K(\vec{x})$. Thus, independent manipulation of α_t, as done here, is somewhat simplistic.

Plots of the second moments $\langle\mu_{200}\rangle$ and $\hat{\mu}_{200}$ (not shown in this paper) for the above two scenarios weakly suggest that as either I_z or α_t becomes large then $\hat{\mu}_{200}$ tends to behave as $\langle\mu_{200}\rangle$; the evidence for this behavior from these plots, however, is not overwhelming. Although increasing either of these quantities tends to decrease S_{200}, this decrease doesn't cause sufficient change in either the behavior of $\langle\mu_{200}\rangle$ or $\hat{\mu}_{200}$ to enable one to state, without reservation, that $\langle\mu_{200}\rangle$ represents this asymptote. From (10), one would expect that, should one drive S_{200} to zero by some process, then $\langle\mu_{200}\rangle$ and $\hat{\mu}_{200}$ would be identical. As $\langle\mu_{200}\rangle$ represents cloud behavior without dispersion of the cloud centroid, it also should represent the resulting asymptotic behavior of this process. In any case, unless the source size is very large, it is unlikely that S_{200} will be zero; if $S_{200}(t)$ is initially nonzero, then it is doubtful that a mechanism exists by which it can be made zero asymptotically.

Ergodicity and the Effective Longitudinal Macrodispersivity

Both Figures 15 and 17 indicate that the coefficient of variation for the x-direction second moment, μ_{200}, decreases with increased travel time $t\langle V_c\rangle/\hat{\lambda}_x$. This result indicates that, with increased travel time, the mean of μ_{200} dominates over its standard deviation and, relatively, μ_{200} becomes less variable. However, the estimated coefficient of variation for μ_{200} does not decrease in every case; $C_v[\mu_{200}]$ can exhibit a contrary behavior as depicted in Figure 18 where $C_v[\mu_{200}]$ is plotted against $t\langle V_c\rangle/\hat{\lambda}_x$ for various values of $\hat{\sigma}_f^2$. When $\hat{\sigma}_f^2$ is less than 0.2, this figure indicates that $C_v[\mu_{200}]$ increases slightly or remains constant as a function of travel time. We suspect, however, that this contrary behavior either may either reflect difficulty in estimating the variance in μ_{200} when this variance is small or reflect the small number of realizations used in these MC simulations. For $\hat{\sigma}_f^2$ greater than 0.2, then $C_v[\mu_{200}]$ does decrease with travel time, but the rate of decrease falls markedly after a travel distance of approximately nine length scales λ_x. Whether this result indicates that a sill has been reached with respect to the amount of decrease in $C_v[\mu_{200}]$ with travel time is debatable; more probable is that this behavior is an artifact of the numerics of estimating these higher order moments.

Because the means of M_{100} and μ_{200} increase more rapidly than their standard deviations as travel time increases, normalized variables $M_{100}/\langle M_{100}\rangle$ and $\mu_{200}/\langle\mu_{200}\rangle$ appear to become less volatile. For $\hat{\mu}_{200}$ and $\langle\mu_{200}\rangle$ to become equal as travel time increases, it is necessary for $S_{200}(t)$ to go to zero as well; however, $S_{200}(t)$ is generally observed to be an increasing function of travel time. As demonstrated in Figure 19, where $S_{200}(t)$ is plotted as a function of dimensionless travel time for different values of α_t (scenario 4), it is unlikely that $S_{200}(t)$ will approach zero with increasing travel time; rather, a more likely scenario is that $S_{200}(t)$ will become asymptotically constant and that Γ_{xx}, representing the slope of $S_{200}(t)$, will approach zero as travel time increases. If this does occur, Figure 19 indicates

that it must do so at travel distance greater than $11\hat{\lambda}_x$. As discussed earlier, the central moments associated scenario 4 exhibit an apparent delay in the development of late-time asymptotic behavior; if this be the case, then this figure may not be representative of the temporal behavior of $S_{200}(t)$ either. Figure 20 is a plot of $S_{200}(t)$ as a function of dimensionless travel time for various values of $\hat{\sigma}_f^2$. Note that the $S_{200}(t)$ curve for $\hat{\sigma}_f^2 = 0.874$ precisely explains the difference between $\langle \mu_{200} \rangle$ and $\hat{\mu}_{200}$ of Figure 5c, as is to be expected. These curves indicate that, for small values of $\hat{\sigma}_f^2$, there is a tendency for $S_{200}(t)$ to approach a positive constant value when $t\langle V_c \rangle / \hat{\lambda}_x \approx 10$ or larger. That is, the growth rate in the plume centroid variance decreases as a function of travel time. On the other hand, in the extreme event that $\hat{\sigma}_f^2 = 0.874$, no relaxation in the growth rate of $S_{200}(t)$ is observed. This centroid variance also has the least maximum travel distance of all the σ_f^2 scenarios; it is probable that, given a larger medium, even the larger $\hat{\sigma}_f^2$ curves would show signs of becoming constant (although a very considerable travel time would probably be required). Thus, although it is unlikely that $\hat{\mu}_{200}$ and $\langle \mu_{200} \rangle$ become equal with increased travel time, there is a reasonable expectation that $A'_{xx} \to A_{xx}$ as $t\langle V_c \rangle / \lambda_x \to \infty$. Supposing that $M_{100}/\langle M_{100} \rangle \to 1$ and $\mu_{200}/\langle \mu_{200} \rangle \to 1$ as $t\langle V_c \rangle / \lambda_x \to \infty$, one can envision that, given sufficient travel time, a single realization of a cloud will tend to behave as the mean cloud in which the distortion for the variance in mean centroid has been removed. Note that even when α_t is very large, there must still exist an initial period, however small, in which the cloud grows to encompass sufficient medium for an ergodic average to be obtained. When I_z is very large, then initially $A'_{xx} \approx A_{xx}$; however, because $C_v[\mu_{200}](t)$ is also large, one must still expect that some travel time will pass before μ_{200} behaves as $\langle \mu_{200} \rangle$.

Regardless of the scheme by which these ergodic effects are achieved, it is most likely that the effective macrodispersivity A_{xx} will best explain the long-term longitudinal spreading of the tracer cloud. The pseudodispersivity Γ_{xx}, as indicated in (25), represents the correction factor for obtaining the effective dispersivity from the mean-cloud dispersivity A'_{xx}. If we assume that the maximum slope of the $S_{200}(t)$ curves of Figure 20 represent this quantity, then an estimate of this correction factor can be approximated; this result is illustrated in Figure 21. This curve closely approximates the difference between A'_{xx} and A_{xx} of Figure 3c. Note that the indicated quadratic fit for these data (Figure 21) suggest that the relation between Γ_{xx}/λ_x and σ_f^2 is of the form $1 - exp(-\sigma_f^2/2)$ and, in fact, this exponential relation is a reasonable approximation of the pseudodispersivity results plotted in Figure 21. Unfortunately, for the same parameter values, the Γ_{xx} value suggested by Figure 16 is almost three times smaller than that shown in Figure 21. Given the above information, one can conjecture that a relation for Γ_{xx} might be defined as

$$\Gamma_{xx} \;=\; \lambda_x J(r)\left[1 - e^{-\sigma_f^2/2}\right] \tag{28}$$

where $J(r)$ is a correction for local dispersion α_t and statistical anisotropy λ_x/λ_z based roughly on the exponential fit illustrated in Figure 16. Given the previously conjectured relation for A'_{xx} (equation (24)), the effective longitudinal macrodispersivity A_{xx} would be defined as

$$A_{xx} - \alpha_\ell \;=\; \lambda_x[2I(r) - J(r)]\left[1 - e^{-\sigma_f^2/2}\right] \tag{29}$$

where $I(r)$ is defined as in equation (21). As noted previously, $I(r) \to 1$ as $r \to 0$; if we also insist that $[2I(r) - J(r)] \to 1$ as $r \to 0$, then $J(r)$ would be of the form

$$J(r) \;=\; 1 - 1.116r + 0.9152r\left[1 - e^{-1.4r}\right] \tag{30}$$

which results from normalizing the exponential fit illustrated in Figure 16. That $[2I(r) - J(r)] \rightarrow 1$ as $r \rightarrow 0$ should reflect the ideal case where local dispersion is neglected; it basically suggests that, when local dispersion is neglected, the effective longitudinal macrodispersivity should be half the mean-cloud longitudinal macrodispersivity. The pseudodispersivity Γ_{xx}, as defined in (28) above, will be slightly smaller, by a factor of about 0.7, than that illustrated in Figure 21, but considerably larger, by a factor of about two, than that given in Figure 16. This weighting may not be unreasonable as the data from scenario 1 (variable σ_f^2) have generally indicated more reliability in their behavior. Although (29) is largely conjectural, based on surmised extensions of some analytical results, it does give a good fit to the estimated effective longitudinal macrodispersivities for scenario 1 (Figure 22). That $J(r)$ is based solely on data from scenario 4 probably causes it to be somewhat biased; a better representation might possibly have been obtained by using all Γ_{xx} data from scenarios 2, 3 and 4 as a basis for the exponential fit. However, given that the dimensionless parameter $r = \alpha_t/\lambda_z \cdot \lambda_x/\lambda_z$ is likely to compensate only approximately for both local transverse dispersion and statistical anisotropy, and also given the overall quality of the data, excessive manipulation is not warranted. Principally, it is the possibility of such a relation that we wish to illustrate.

Non-Gaussian Effects

Because the hydraulic conductivity field for each realization of a MC simulation is generated from a log-normal distribution, it cannot be expected that, at least in the x-direction, the velocity field will be normally distributed. Without a Gaussian velocity field, it is improbable that the mean cloud will exhibit a Gaussian behavior [e.g., *Dagan*, 1987], except possibly in large time. Departure from Gaussian behavior represents a non-ideality in the mean cloud insofar as the standard advective dispersion equation assumes that the spatial distribution of the tracer cloud is Gaussian, or at least that the plume results from a process that is Gaussian in nature. In this section, we briefly examine the average non-Gaussian character of the tracer cloud by examining the third central moment of the mean cloud in the mean flow direction.

The third central moment of the mean cloud in the x-direction, $\hat{\mu}_{300}(t)$, is defined in a manner analogous to $\hat{\mu}_{200}(t)$ of equation (9). The coefficient of skewness, C_s, is defined herein as this quantity normalized by the equivalent second central moment, $\hat{\mu}_{200}(t)$, raised to the three-halves power: $C_s(t) = \hat{\mu}_{300}(t)/\left[\hat{\mu}_{200}(t)\right]^{3/2}$. For a symmetric distribution, such as the normal, the skewness coefficient is expected to be zero. Because all moments must be estimated and as the error in estimation increases with the degree of the moment, small values for the magnitude of the skewness coefficients ($|C_s| << 1$) are considered to be indicative of a Gaussian distribution. The coefficient of skewness, as a function of travel time and $\hat{\sigma}_f^2$ (scenario 1), is shown in Figure 23; here $\hat{\lambda}_x = 2.77\ m$, $\hat{\lambda}_y = 2.79\ m$, $\hat{\lambda}_z = 0.278\ m$, $\alpha_\ell = 0.1\ m$ and $\alpha_t = 0.01\ m$. (For reasons of clarity, some curves for values of $\hat{\sigma}_f^2$ presented in earlier figures have been eliminated from this figure.) It is apparent from this figure that the mean cloud is, at least initially, positively skewed and that, for any given time, the coefficient of skewness is generally an increasing function of $\hat{\sigma}_f^2$. This figure suggests

that when $\hat{\sigma}_f^2$ is sufficiently small a Gaussian-like behavior of the mean cloud will dominate at all travel time. This result agrees in principle with first-order analyses, where σ_f^2 is assumed small; these analyses indicate that, under first-order conditions, a Gaussian behavior should be prevalent [e.g., *Dagan*, 1984; *Naff*, 1990]. The skewness of the mean cloud also decreases with travel time and, provided $\hat{\sigma}_f^2$ is about 0.6 or less, a travel time equivalent to about seven to eight length scales is sufficient to reduce C_s from its peak value to a value less than one. For large values of σ_f^2, this figure suggests that significant travel times will be required for a Gaussian behavior to be achieved.

As noted previously, increasing the local transverse dispersivity α_t has the effect of smoothing the tracer cloud, causing it to be less variable. Increasing α_t also acts to diminish the skewness of the mean cloud. Figure 24 is a plot of $C_s(t)$ as a function of dimensionless travel time and α_t for MC scenario 4 where $\hat{\lambda}_x = 2.78\ m$, $\hat{\lambda}_y = 2.79\ m$, $\hat{\lambda}_z = 0.278\ m$, and $\hat{\sigma}_f^2 = 0.527$; α_ℓ was held constant at $0.1\ m$. Results shown in this figure are for the 20 realization simulation. A curve for $\alpha_t = 0.05\ m$ was not plotted on this figure for clarity; had it been plotted, it would appear similar to the curve for $\alpha_t = 0.035\ m$ for the $10\hat{\lambda}_x$ of travel time present. Note that, unlike the previous plot for variable σ_f^2, these curves initially decrease with travel time and then subsequently increase to their maximum skewness. This behavior is believed to be related to the aforementioned delayed development of the tracer cloud; it is only after six length scales travel distance that the skewness of the mean cloud begins to behave as expected. We suspect, because of this apparent delay, the very late-time behavior of $C_s(t)$ for this MC scenario is missed. Over the observed travel time, larger values of α_t generally result in mean clouds with significantly smaller positive skews. That the results for $\alpha_t = 0.035\ m$ and $\alpha_t = 0.05\ m$ are similar suggests that there may exist a limit on the decrease in skewness one can obtain from simply increasing α_t. One may speculate that this limit is related to the development of the transverse macrodispersive A_{zz}. As

noted previously, when α_t exceeds $0.035\ m$ then A_{zz} is apparently composed entirely of α_t. However, it is not clear that a causal connections exists.

Estimated skewness coefficients in other than the longitudinal direction are generally small, probably on the order of the error in their estimation. Thus, it is expected that the transverse spatial moments will follow a Gaussian model.

Discussion and Conclusions

Perhaps the most surprising aspect of this investigation was the considerable variability encountered in the duration of the preasymptotic behavior of the second moments $\langle\mu_{200}\rangle$, $\langle\mu_{020}\rangle$ and $\langle\mu_{002}\rangle$. Because the initial concentration zone is small relative to the vertical length scale, some variability was expected; indeed the earlier study by *Burr et al.* [1994] also encountered similar difficulties. One's intuition is that, as the number of realizations increased, this problem would be minimized. We suspect that the preasymptotic behavior of these second moments is particularly sensitive to any slight bias in the hydraulic conductivity field immediately downgradient of the initial concentration zone. Our decision to condition these simulations on a certain range of hydraulic conductivities for the source box may have contributed to this sensitivity [*Naff et al.*, this issue]. However, because of complications concerning the use of computational facilities, we were not able to repeat any of these simulations to verify this surmise. We also note that, in general, the moment estimates contained in this study would most probably have benefited from the use of more realizations in each Monte-Carlo simulation; we suspect that if 80 rather than 20 realizations had been used in each simulation, than comparisons between simulations from differing random field sets would have been more acceptable. Finally, the estimation procedure used in this study to obtain late-time macrodispersivities were subjective in that it entailed discerning the late-time linear behavior of the second-moment curves. In most cases, second-moment curves exhibited at least apparent linear behavior at large travel time ($\sim 10\lambda_x$); however, one cannot rule out the possibility that, had a larger domain been used in this study, yet another behavior would have been observed. We believe that the late-time macrodispersivity estimates contained herein are at least indicative of the true macrodispersivity values for the various senarios, although they may not be as precise as we had desired.

Several closed forms were investigated for estimating the mean-cloud longitudinal macrodispersivity $A'_{xx} - \alpha_\ell$. Over the range of values for the variance in log hydraulic conductivity σ_f^2 used in this study ($\sigma_f^2 \leq 0.9$), forms which correct for the effects of local transverse dispersion and which incorporate a second-order correction appear to be most appropriate to explain the observed values of $A'_{xx} - \alpha_\ell$. The form used in this study to correct for the effects of local dispersion ($I(r)$ of (21) used in conjunction with (24)) does not appear to be entirely adequate for the entire range of local transverse dispersivities α_t and statistical anisotropies λ_x/λ_z used in this investigation. While the use of a single dimensionless parameter $r = \alpha_t/\lambda_z \cdot \lambda_x/\lambda_z$ seemingly works well for small values of r, deviations become more apparent as r increases, either by increasing the statistical anisotropy (Figure 10) or local transverse dispersivity α_t (Figure 13). It probably is not possible to develop a higher order correction based on the single dimensionless parameter r as the departures from the Monte-Carlo simulations resulting from increasing λ_x/λ_z and α_t are not consistent. That is, equation (22) or (24) tends to underestimate Monte-Carlo simulation results as λ_x/λ_z increases (Figure 10), but overestimate as α_t increases (Figure 13).

Because of the limitations on the domain size used in theses Monte-Carlo simulations, any single realization simulation did not allow the plume to sample the heterogeneous nature of the medium in the y direction as much as one would desire. As a result the transverse macrodispersivity estimates for this direction are probably inferior to those for the z; we suspect that this is the reason that scenario 4 depicts A'_{yy} and A_{yy} as being essentially idential (Figure 12), while scenario 1 indicates that $A'_{yy} > A_{yy}$. The analytical results of *Zhang and Neuman* [1990], using a variant of Corrsin's conjecture [*Neuman and Zhang*, 1990], appear to best approximate, for σ_f^2 of the order 0.9, the mean-cloud transverse macrodispersivities A'_{yy} and A'_{zz} observed in this investigation. Their equivalent estimator for the longitudinal macrodispersivity, $A'_{xx} - \alpha_\ell$, produces, for $\sigma_f^2 \sim 0.9$, not unreasonable agreement with the results depicted in Figure 4 [*Zhang and Neuman*, 1990, Figure 1].

However, Figures 3 and 4 indicate that the observed macrodispersivities are, at best, only weakly nonlinear functions of σ_f^2, while the results of *Zhang and Neuman* [1990] suggest that they should be strongly nonlinear functions. It does appear that a weak interaction between local dispersion and the variable velocity field is responsible for the transverse macrodispersion observed in this study.

When the local transverse dispersivity α_t is small, a z-direction transverse macrodispersion two to three times greater than α_t is possible (Figure 3b). However, if α_t is made large then transverse macrodispersion is dominated almost entirely by the transverse component of local dispersion (Figure 12b); that is, A_{zz} becomes identical to α_t. Also, when $\hat{\lambda}_x$ increases, the transverse macrodispersivities A_{yy} and A_{zz} tend to decrease (Figures 7a and 7b). Thus one might speculate as to whether approximations for A_{yy} and A_{zz} might not also be based on the dimensionless parameter $r = \alpha_t/\lambda_z \cdot \lambda_x/\lambda_z$. To vary α_t independently of the other parameters, as done in this study, is probably not entirely realistic; most likely α_t is related indirectly to the mean and variance in hydraulic conductivity. That is, the local dispersivity itself is a spatial variable whose mean, α_t, is constrained by the medium hydraulic conductivity parameters. As a result, application of such large mean values of α_t in these flow and transport scenarios may be unrealistic.

It appears likely that, as the plume disperses and grows with travel time, the mean-cloud macrodispersivity A'_{xx} tends to the effective macrodispersivity A_{xx} and that the pseudodispersivity Γ_{xx} tends to become null; that is, given sufficient travel time, variability associated with the the cloud centroid ceases to contribute to the mean-cloud second moment $\hat{\mu}_{200}$, and the slope of this second moment approaches that of the mean-realization second moment $\langle\mu_{200}\rangle$. This process appears to be aided either by increasing the vertical dimension of the source or by increasing the local transverse dispersivity. Since few expressions are hypothesized for the effective longitudinal dispersivity A_{xx}, we provide one herein

based on these Monte-Carlo results (equation (29)). While increasing the local transverse dispersivity α_t and the vertical dimension of the source box I_z both serve to diminish the plume centroid variability in the x direction, only increasing α_t causes the coefficient of variation in the second moment μ_{200} to be diminished. On the other hand, increasing the source size dimension appears to be particularly effective at diminishing the magnitude of S_{200} from onset of plume development. Over the limited range tested in this investigation, increasing I_z does not cause a realization's second moment, μ_{200}, to behave like its mean; on the contrary, one would expect an even greater departure from mean behavior by any single realization estimate of μ_{200}. One caveat to these interpretations should be added: most of the significant ergodic behavior based on travel time would occur at distances beyond that which could be modelled with these Monte-Carlo simulations. Commonly, only the earliest tendency toward an ergodic behavior in these moments was observed in this study.

Unless the medium is particularly uniform, it is to be expected that the average cloud will exhibit positive skewness for a travel distance of at least seven to eight length scales λ_x; for media that is particularly variable, the mean cloud may be even more persistently non-Gaussian. These nonidealities are important in that they are reflected in the tail behavior of every cloud; a positively skewed cloud may have the same travel time as a Gaussian cloud, but the arrival time at a distant point of a significant portion of the tracer cloud may be well in advance of that predicted by a Gaussian cloud. Should an aquifer exhibit significant variability, it may be expected that significant quantities of the tracer could arrive at downgradient locations faster than predicted by the standard advective dispersion equation.

Acknowledgments

We wish to thank the National Center for Atmospheric Research at Boulder, Colorado, for having given us time on a Cray-3 supercomputer; without this resource, it is unlikely that this study could have been completed. We also wish to thank all the former employees of Cray Computer Corporation for all the assistance lent to make our model work efficiently on this machine. Gilbert Barth and Steen Christensen provided critical reviews in early drafts of this two-part paper.

References

Abramowitz, M., and I.A. Stegun, *Handbook of Mathematical Functions*, Dover, 1972.

Bellin, A., P. Salandin, and A. Rinaldo, Simulation of dispersion in heterogeneous porous formations, *Water Resour. Res.*, 28(9), 2211-2227, 1992.

Burr, D.T., E.A. Sudicky and R.L. Naff, Nonreactive and reactive solute transport in three-dimensional heterogeneous media: Mean displacement, plume spreading and uncertainty, *Water Resour. Res.*, 30(3), 791-815, 1994.

Chin, D.A., and T. Wang, An investigation of first-order stochastic dispersion theories in isotropic porous media, *Water Resour. Res.*, 28(6), 1531-1542, 1992.

Dagan, G., Solute transport in heterogeneous porous formations, *J. Fluid Mech.*, 145, 151-177, 1984.

Dagan, G., Theory of solute transport by groundwater, *Ann. Rev. Fluid Mech.*, 19, 183-215, 1987.

Dagan, G., Time-dependent Macrodispersion for solute transport in anisotropic heterogeneous aquifers, *Water Resour. Res.*, 24(9), 1491-1500, 1988.

Dagan, G., Transport in heterogeneous porous formations: spatial moments, ergodicity, and effective dispersion, *Water Resour. Res.*, 26(6), 1281-1290, 1990.

Dagan, G, Dispersion of a passive solute in non-ergodic transport by steady velocity fields in heterogeneous formations, *J. Fluid Mech.*, 233, 197-210, 1991.

Dagan, G., An exact nonlinear correction to transverse macrodispersivity for transport in heterogeneous porous formations, *Water Resour. Res.*, 30(10), 2699-2705, 1994.

Desai, C.S., and J.F. Abel, *Introduction to the Finite Element Method*, Van Nostrand Reinhold, 1972.

Gelhar, L.W., and C.L. Axness, Three-dimensional stochastic analysis of macrodispersion in a stratified aquifer, *Water Resour. Res.*, 19(1), 161-180, 1983.

Gradshteyn, I.S., and I.M. Ryzhik, *Table of Integrals, Series, and Products*, Academic Press, 1965.

Harter, T., and T.-C. Jim Yeh, Stochastic analusis of solute transport in heterogeneous, variably saturated soils, *Water Resour. Res.*, 32(6), 1585-1595, 1996.

Jussel, P., F. Stauffer, and T. Dracos, Transport modeling in heterogeneous aquifers: 2. Three-dimensional transport model and stochastic numerical tracer experiment, *Water Resour. Res.*, 30(6), 1819-1831, 1994.

Naff, R.L., On the nature of the dispersive flux in saturated heterogeneous porous media, *Water Resour. Res.*, 26(5), 1013-1026, 1990.

Naff, R.L., An Eulerian scheme for the second-order approximation of subsurface transport moments, *Water Resour. Res.*, 30(5), 1439-1455, 1994.

Naff, R.L., D.F. Haley and E.A. Sudicky, High-resolution Monte-Carlo simulation of flow and conservative transport in heterogeneous porous media: 1, methodology and flow results, *Water Resour. Res.*, this issue.

Neuman, S.P., and Y.-K. Zhang, A quasi-linear theory of non-Fickian and Fickian subsurface dispersion 1. Theoretical Analysis with application to isotropic media, *Water Resour. Res.*, 26(5), Resour.887-902, 1990.

Rajaram, H., and L.W. Gelhar, Plume scale-dependent dispersion in heterogeneous aquifers 2. Eulerian analysis and three-dimensional aquifers, *Water Resour. Res.*, 29(9), 3261-3276, 1993.

Sposito, G., and D.A. Barry, On the Dagan model of solute transport in groundwater: Foundational aspects, *Water Resour. Res.*, 23(10), 1867-1875, 1987.

Tompson, A.F.P., Numerical simulation of chemical migration in physically and chemically heterogeneous porous media, *Water Resour. Res.*, 29(11), 3709-3726, 1993.

Tompson, A.F.P., and L.W. Gelhar, Numerical simulation of solute transport in three-dimensional, randomly heterogeneous porous media, *Water Resour. Res.*, 26(10), 2541-2562, 1990.

Zhang, Y.-K., and S.P. Neuman, A quasi-linear theory of non-Fickian and Fickian subsurface dispersion 2. Application to anisotropic media and the Borden site, *Water Resour. Res.*, 26(5), 903-913, 1990.

Zhang, Q., Transient behavior of mixing induced by a random velocity field, *Water Resour. Res.*, 31(3), 577-591, 1995.

Figure Captions

Figure 1. Example x-direction second-moment curves. Dashed lines: individual realizations; solid line: mean of realizations.

Figure 2. Example mean second-moment curves for three principal directions. a: transverse horizontal; b: transverse vertical; c: longitudinal.

Figure 3. Macrodispersivities as a function of variance in log hydraulic conductivity $\hat{\sigma}_f^2$. Mean cloud: A'_{xx}, A'_{yy}, A'_{zz}. Effective: A_{xx}, A_{yy}, A_{zz}.

Figure 4. Mean-cloud longitudinal macrodispersivity as a function of variance in log hydraulic conductivity $\hat{\sigma}_f^2$: Comparison with analytical solutions.

Figure 5. Mean second moments for Monte-Carlo scenario 1 with $\hat{\sigma}_f^2 = 0.349$. a: transverse horizontal; b: transverse vertical; c: longitudinal.

Figure 6. Realization mean macrodispersivities $\langle A''_{xx} \rangle$, $\langle A''_{yy} \rangle$ and $\langle A''_{zz} \rangle$. Dashed lines represent fit to effective macrodispersivities A_{xx}, A_{yy} and A_{zz} of Figure 3.

Figure 7. Macrodispersivities as a function of horizontal length scale $\hat{\lambda}_x$. Mean cloud: A'_{xx}, A'_{yy}, A'_{zz}. Effective: A_{xx}, A_{yy}, A_{zz}.

Figure 8 Normalized longitudinal macrodispersivities as a function of statistical anisotropy $\hat{\lambda}_x/\hat{\lambda}_z$: Monte-Carlo scenario 2.

Figure 9 Normalized longitudinal macrodispersivities as a function of statistical anisotropy $\hat{\lambda}_x/\hat{\lambda}_z$: Monte-Carlo scenario 3.

Figure 10 Normalized mean-cloud longitudinal macrodispersivities as a function of $r = \alpha_t/\hat{\lambda}_z \cdot \hat{\lambda}_x/\hat{\lambda}_z$; Monte-Carlo scenarios 2 and 3.

Figure 11 Second moments for Monte-Carlo scenario 4 with $\alpha_t = 0.01\ m$. Dashed lines: individual realizations; solid line: mean of realizations. *a*: transverse horizontal; *b*: transverse vertical; *c*: longitudinal.

Figure 12 Macrodispersivities as a function of local transverse dispersivity $\hat{\lambda}_x$. Mean cloud: A'_{xx}, A'_{yy}, A'_{zz}. Effective: A_{xx}, A_{yy}, A_{zz}.

Figure 13 Normalized mean-cloud longitudinal macrodispersivities as a function of $r = \alpha_t/\hat{\lambda}_z \cdot \hat{\lambda}_x/\hat{\lambda}_z$; Monte-Carlo scenario 4.

Figure 14 Pseudodispersivity Γ_{xx} as a function of relative source size $I_z/\hat{\lambda}_x$.

Figure 15 Coefficient of variation for $\mu_{200}(t)$ as a function of relative source size $I_z/\hat{\lambda}_x$ and dimensionless travel time $t\langle V_c\rangle/\hat{\lambda}_x$.

Figure 16 Pseudodispersivity Γ_{xx} as a function of local transverse dispersivity α_t. Also normalized pseudodispersivity $\Gamma_{xx}/\hat{\lambda}_x$ as a function of $r = \alpha_t/\hat{\lambda}_z \cdot \hat{\lambda}_x/\hat{\lambda}_z$.

Figure 17 Coefficient of variation for $\mu_{200}(t)$ as a function of local transverse dispersivity α_t and dimensionless travel time $t\langle V_c\rangle/\hat{\lambda}_x$.

Figure 18 Coefficient of variation for $\mu_{200}(t)$ as a function of variance in log hydraulic conductivity $\tilde{\sigma}_f^2$ and dimensionless travel time $t\langle V_c\rangle/\hat{\lambda}_x$.

Figure 19 Plume centroid variance S_{200} as a function of local transverse dispersivity α_t and dimensionless travel time $t\langle V_c\rangle/\hat{\lambda}_x$.

Figure 20 Plume centroid variance S_{200} as a function of variance in log hydraulic conductivity $\hat{\sigma}_f^2$ and dimensionless travel time $t\langle V_c\rangle/\hat{\lambda}_x$.

Figure 21 Pseudodispersivity Γ_{xx} as a function of variance in log hydraulic conductivity $\hat{\sigma}_f^2$.

Figure 22 Effective longitudinal macrodispersivity A_{xx} as a function of variance in log hydraulic conductivity $\hat{\sigma}_f^2$.

Figure 23 Coefficient of skewness $C_s(t)$ as a function of variance in log hydraulic conductivity $\hat{\sigma}_f^2$ and dimensionless travel time $t\langle V_c\rangle/\hat{\lambda}_x$.

Figure 24 Coefficient of skewness $C_s(t)$ as a function of local transverse dispersivity α_t and dimensionless travel time $t\langle V_c\rangle/\hat{\lambda}_x$.

Figure1

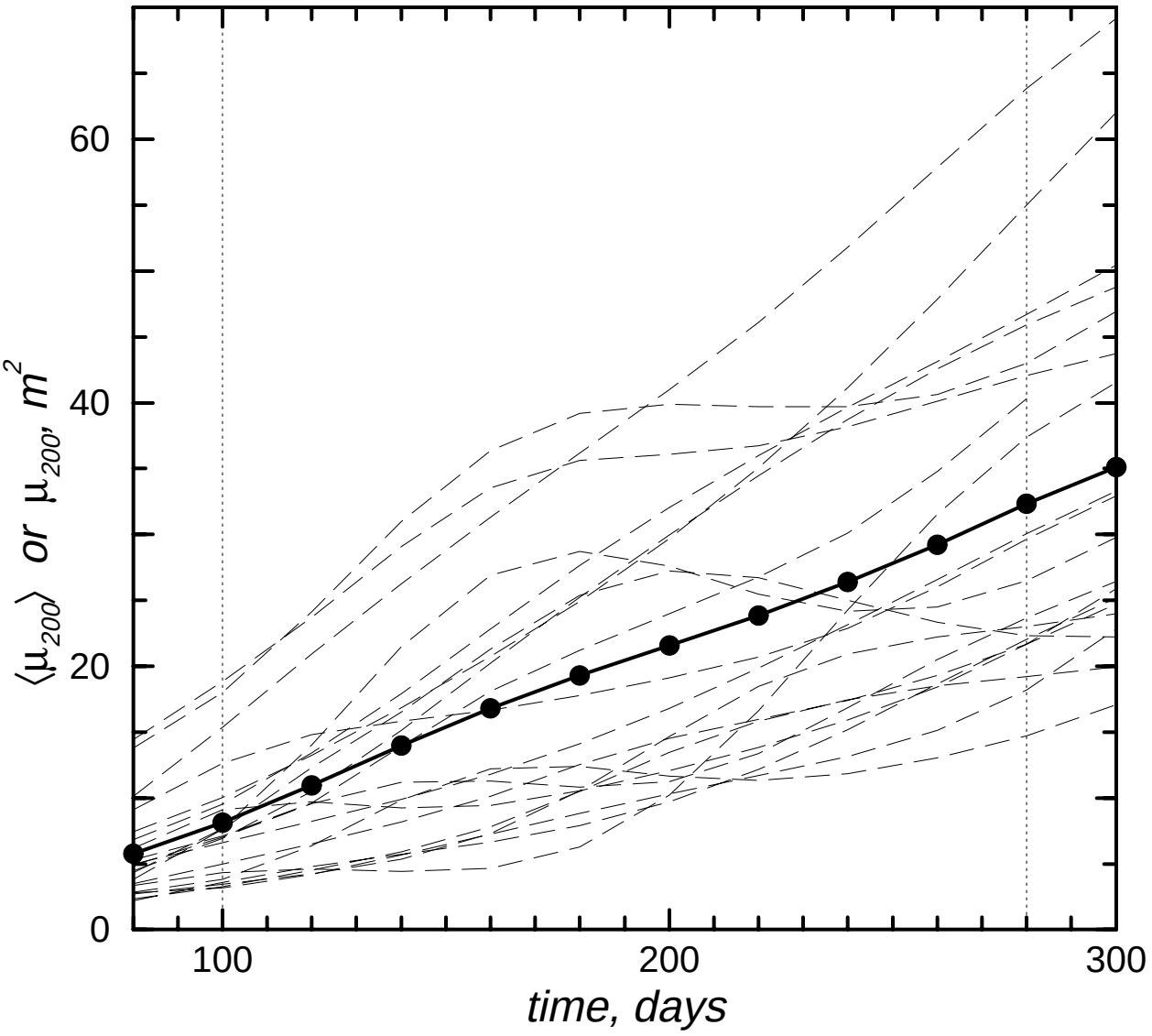

Figure 2

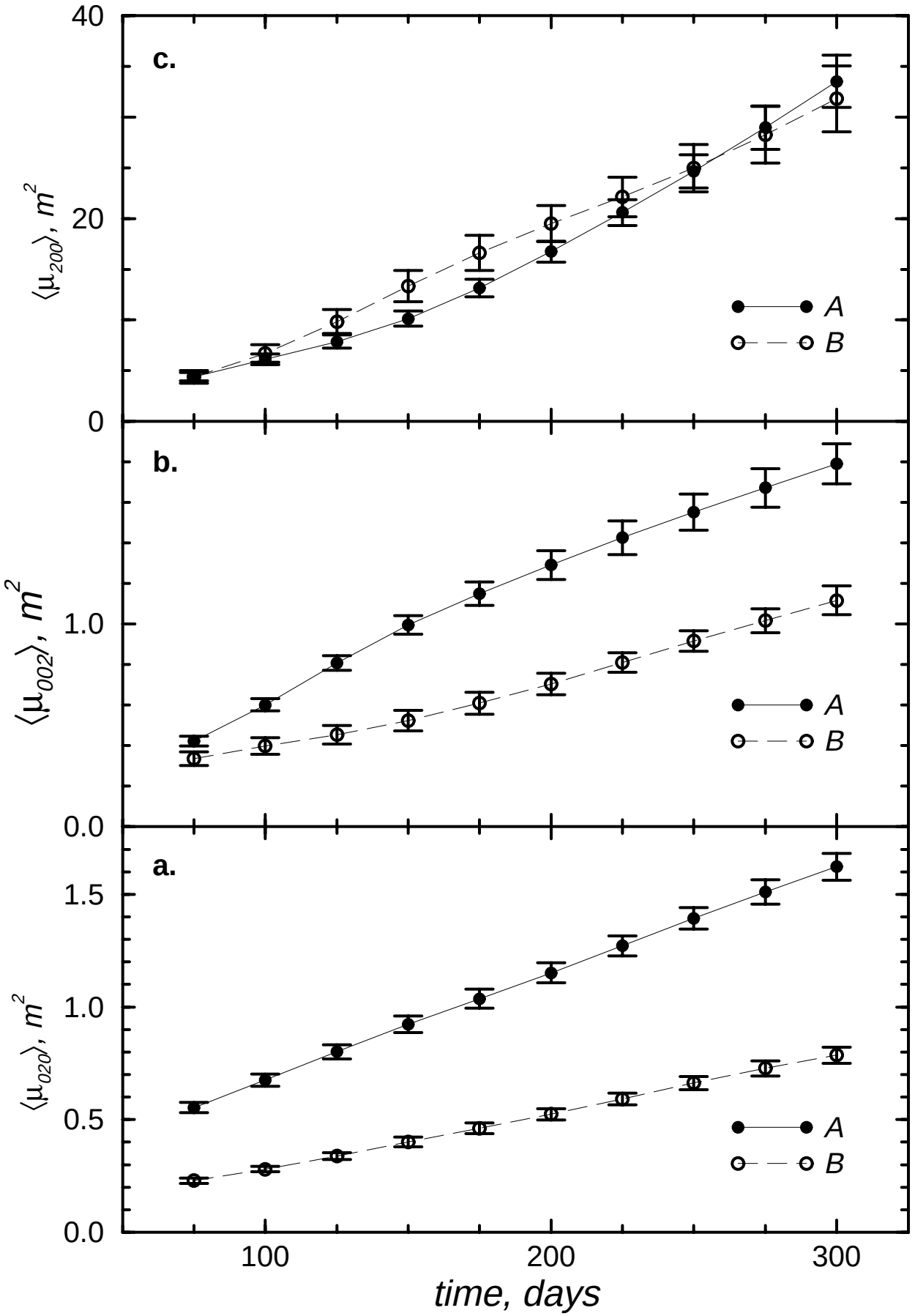
c.
b.
a.
A
B
⟨μ200⟩, m2
⟨μ002⟩, m2
⟨μ020⟩, m2
40
20
0
1.0
0.0
1.5
1.0
0.5
0.0
100
200
300
time, days

Figure 3

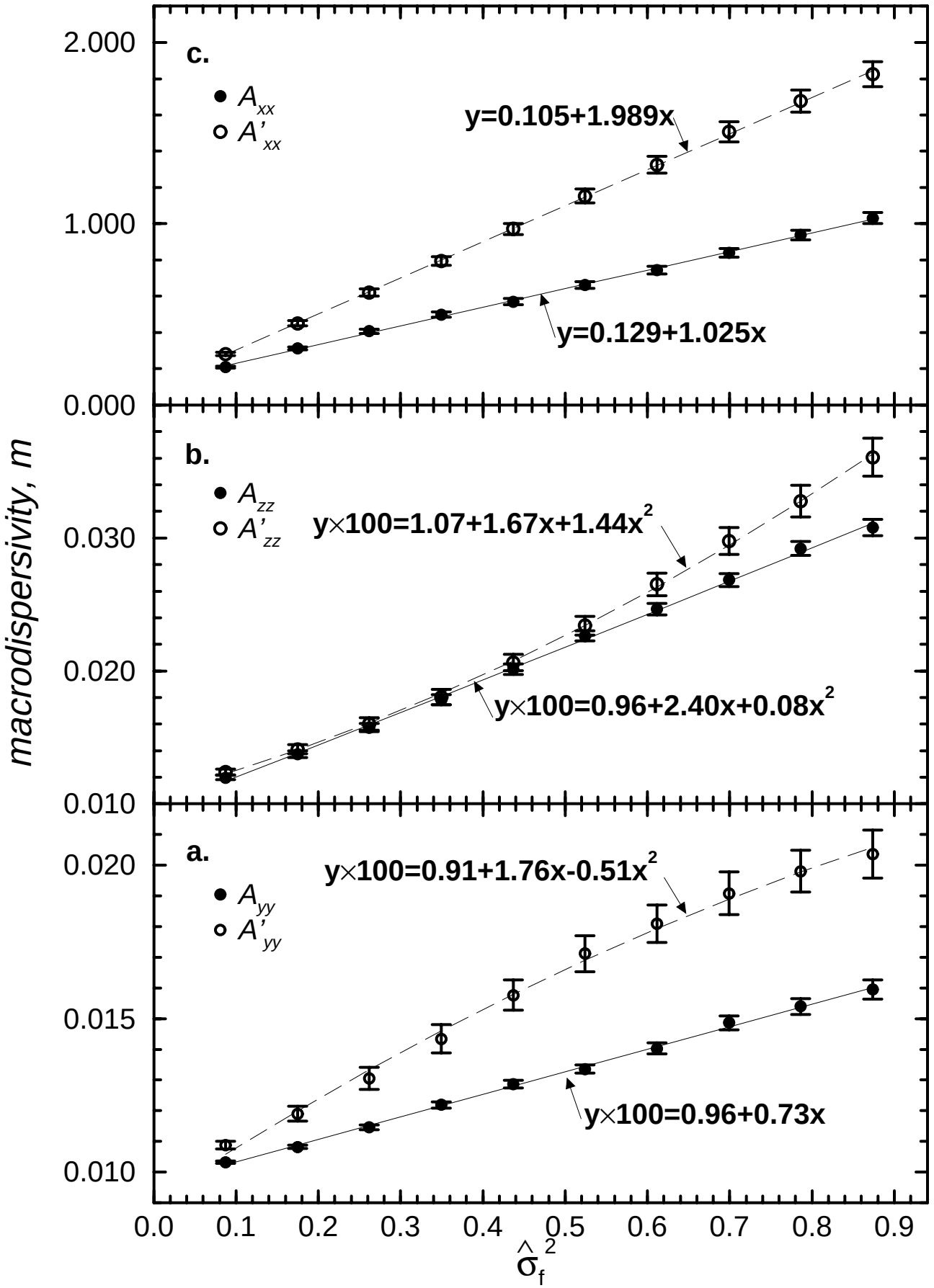
c.
A_{xx}
A'_{xx}
y=0.105+1.989x
y=0.129+1.025x
b.
A_{zz}
A'_{zz}
y×100=1.07+1.67x+1.44x²
y×100=0.96+2.40x+0.08x²
a.
A_{yy}
A'_{yy}
y×100=0.91+1.76x-0.51x²
y×100=0.96+0.73x
macrodispersivity, m
$\hat{\sigma}_f^2$
2.000
1.000
0.000
0.030
0.020
0.010
0.020
0.015
0.010
0.0
0.1
0.2
0.3
0.4
0.5
0.6
0.7
0.8
0.9

Figure 4

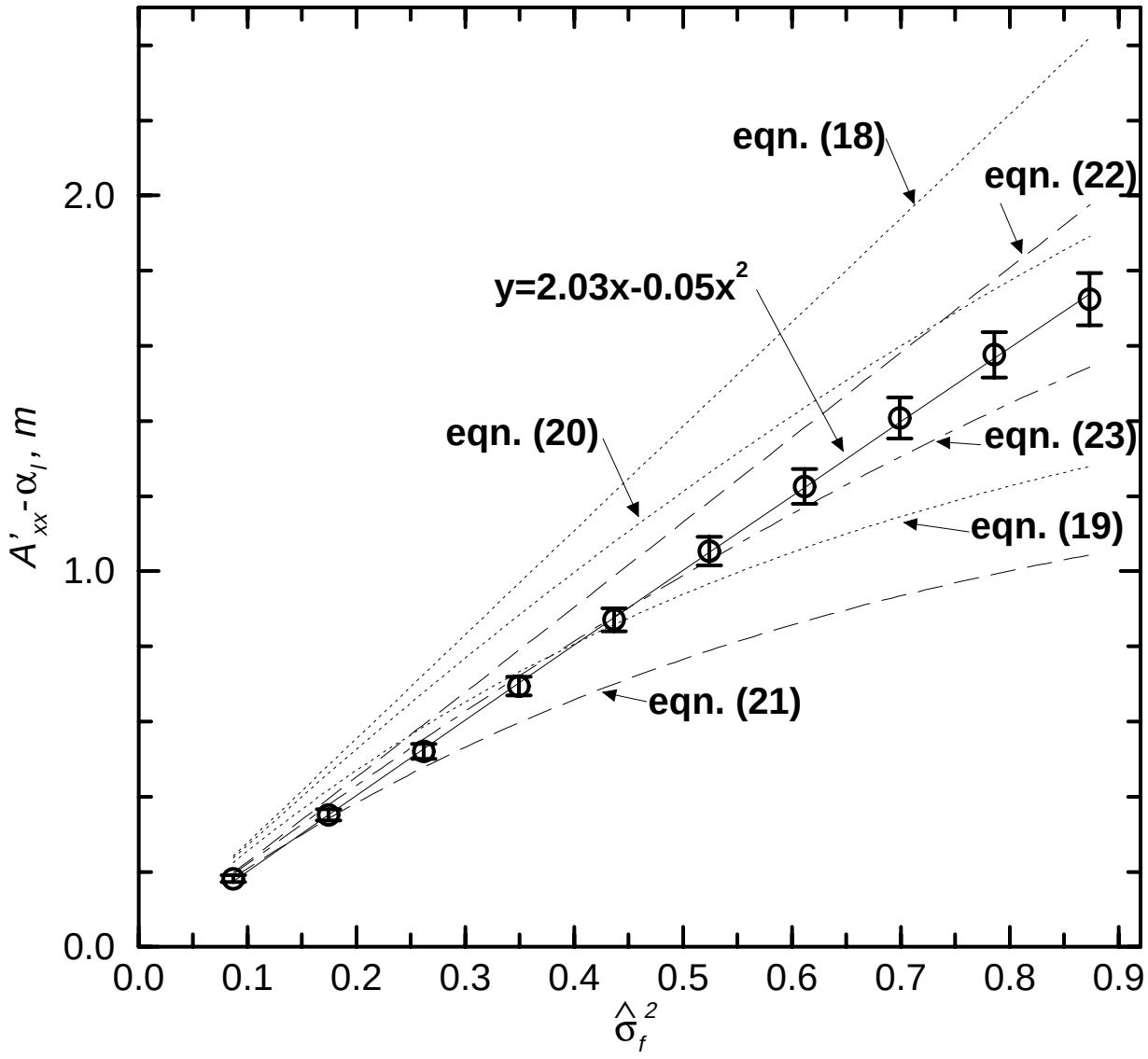
eqn. (18)
eqn. (22)
y=2.03x-0.05x²
eqn. (20)
eqn. (23)
eqn. (19)
eqn. (21)
A'xx-αl, m
σ̂f²
0.0
1.0
2.0
0.0
0.1
0.2
0.3
0.4
0.5
0.6
0.7
0.8
0.9

Figure 5

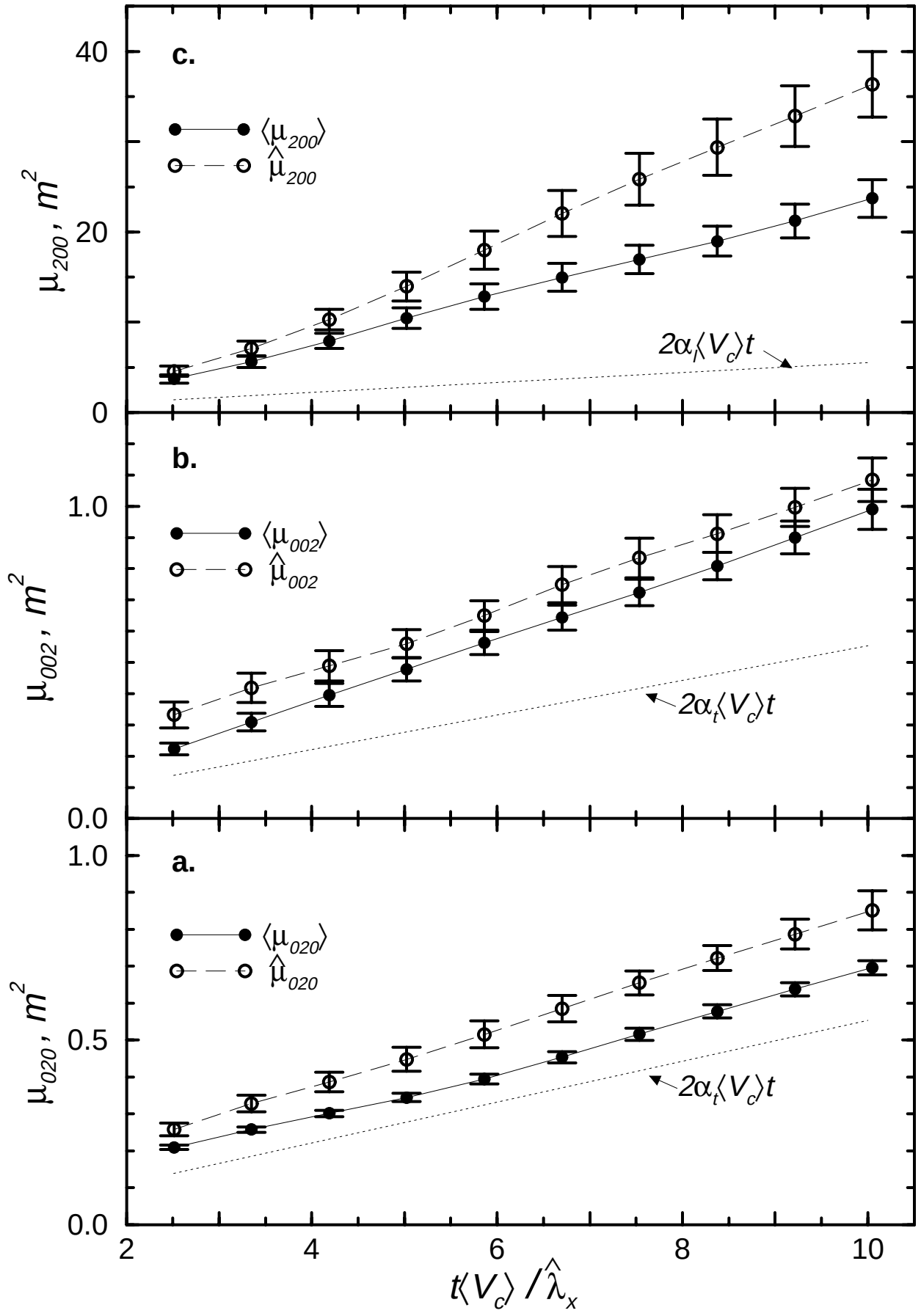
c.
b.
a.
⟨μ200⟩
μ̂200
⟨μ002⟩
μ̂002
⟨μ020⟩
μ̂020
2α_l⟨V_c⟩t
2α_t⟨V_c⟩t
μ200, m2
μ002, m2
μ020, m2
t⟨V_c⟩ / λ̂_x
0
20
40
0.0
1.0
0.5
2
4
6
8
10

Figure 6

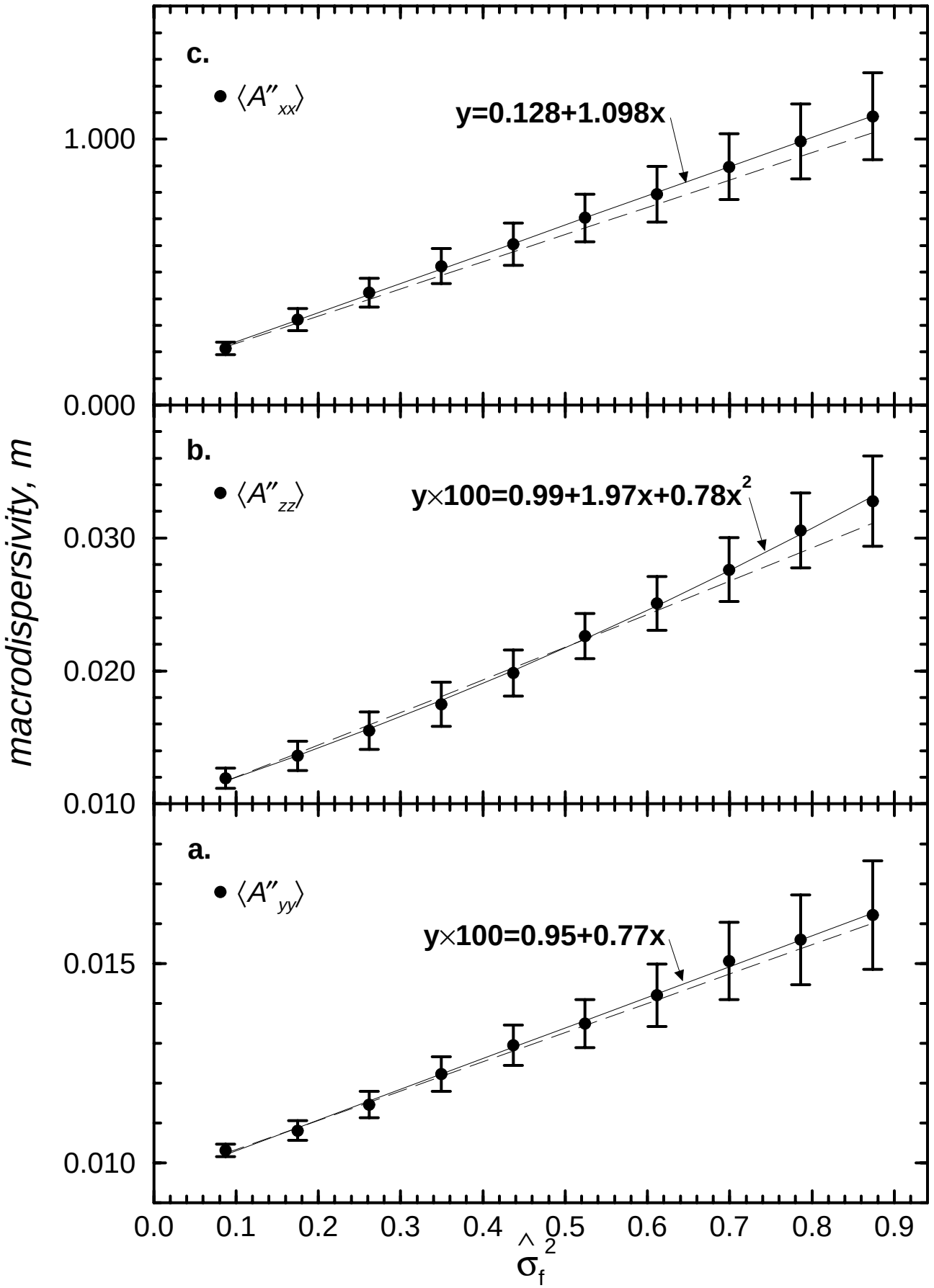
c.
⟨A″xx⟩
y=0.128+1.098x
1.000
0.000
b.
⟨A″zz⟩
y×100=0.99+1.97x+0.78x2
0.030
0.020
0.010
a.
⟨A″yy⟩
y×100=0.95+0.77x
0.015
0.010
macrodispersivity, m
0.0
0.1
0.2
0.3
0.4
0.5
0.6
0.7
0.8
0.9
σ̂f2

Figure 7

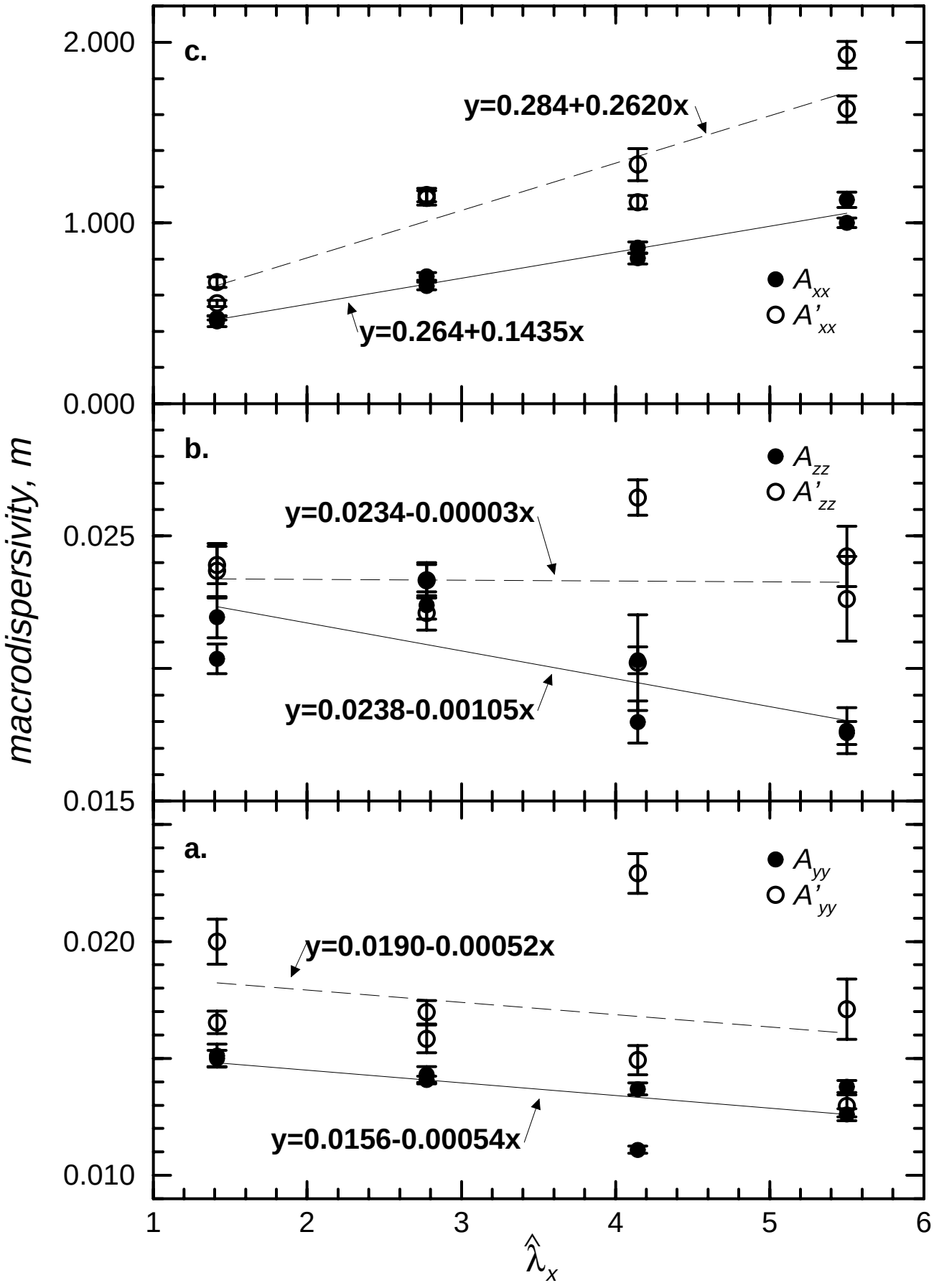
c.
y=0.284+0.2620x
y=0.264+0.1435x
A_{xx}
A'_{xx}
b.
y=0.0234-0.00003x
y=0.0238-0.00105x
A_{zz}
A'_{zz}
a.
y=0.0190-0.00052x
y=0.0156-0.00054x
A_{yy}
A'_{yy}
macrodispersivity, m
$\hat{\lambda}_x$
2.000
1.000
0.000
0.025
0.015
0.020
0.010
1
2
3
4
5
6

Figure 8

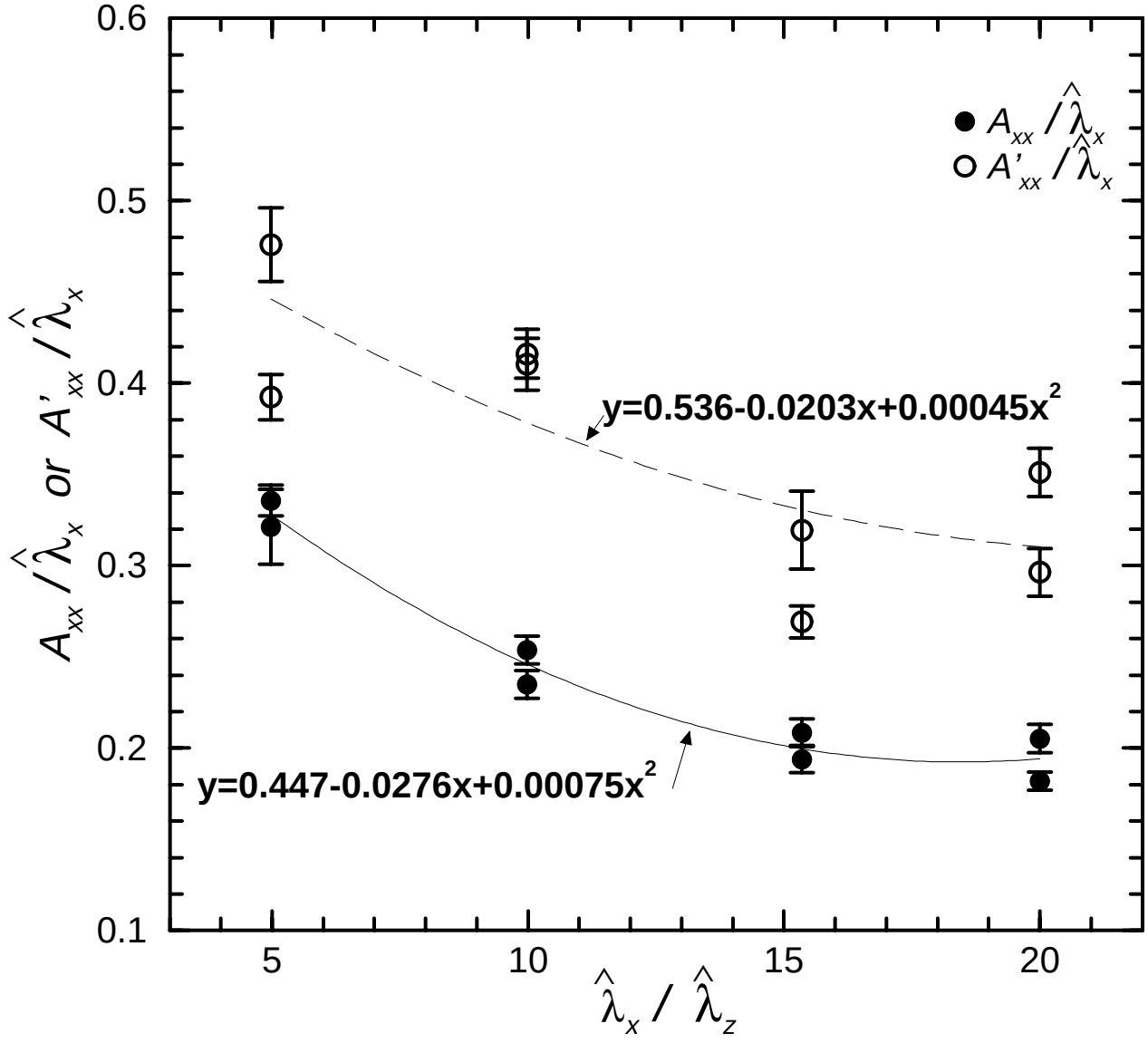
0.6
0.5
0.4
0.3
0.2
0.1
5
10
15
20
$A_{xx} / \hat{\lambda}_x$
$A'_{xx} / \hat{\lambda}_x$
$A_{xx} / \hat{\lambda}_x$ or $A'_{xx} / \hat{\lambda}_x$
$\hat{\lambda}_x / \hat{\lambda}_z$
y=0.536-0.0203x+0.00045x²
y=0.447-0.0276x+0.00075x²

Figure 9

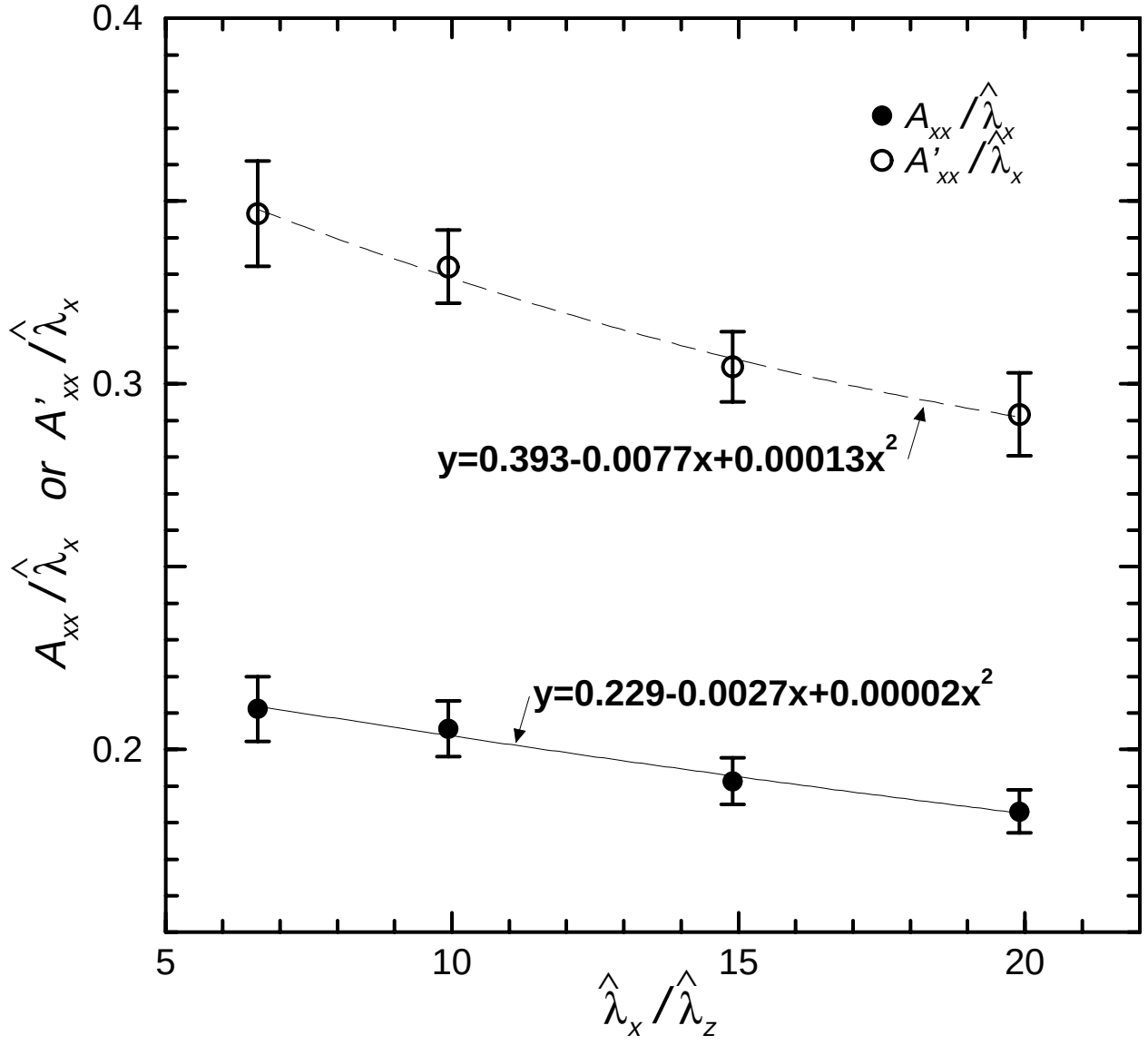
0.4
0.3
0.2
5
10
15
20
$A_{xx}/\hat{\lambda}_x$ or $A'_{xx}/\hat{\lambda}_x$
$\hat{\lambda}_x/\hat{\lambda}_z$
$A_{xx}/\hat{\lambda}_x$
$A'_{xx}/\hat{\lambda}_x$
y=0.393-0.0077x+0.00013x^2
y=0.229-0.0027x+0.00002x^2

Figure 10

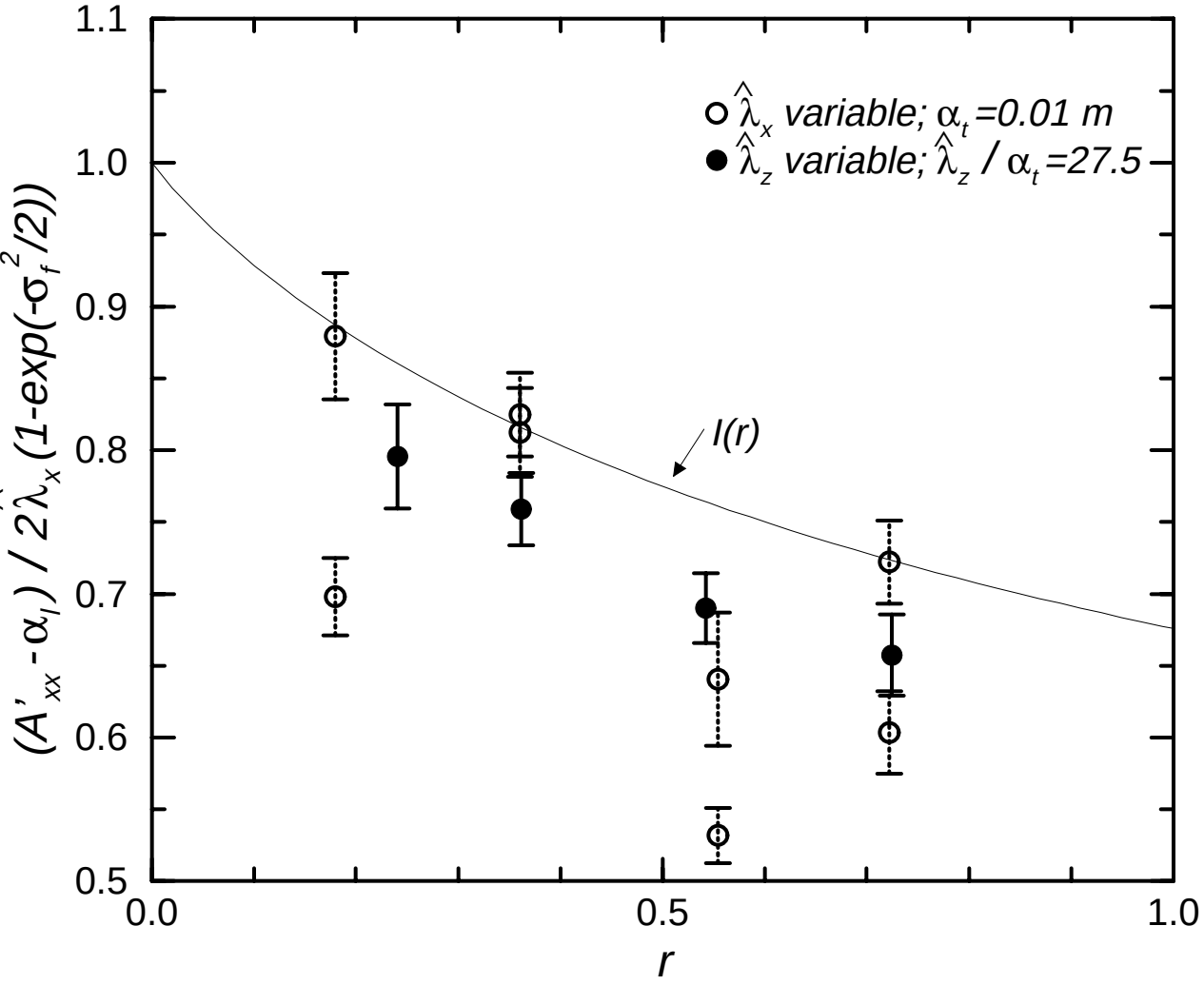
1.1
1.0
0.9
0.8
0.7
0.6
0.5
0.0
0.5
1.0
r
(A'xx - αl) / 2λ̂x (1-exp(-σf2/2))
λ̂x variable; αt =0.01 m
λ̂z variable; λ̂z / αt =27.5
I(r)

Figure 11

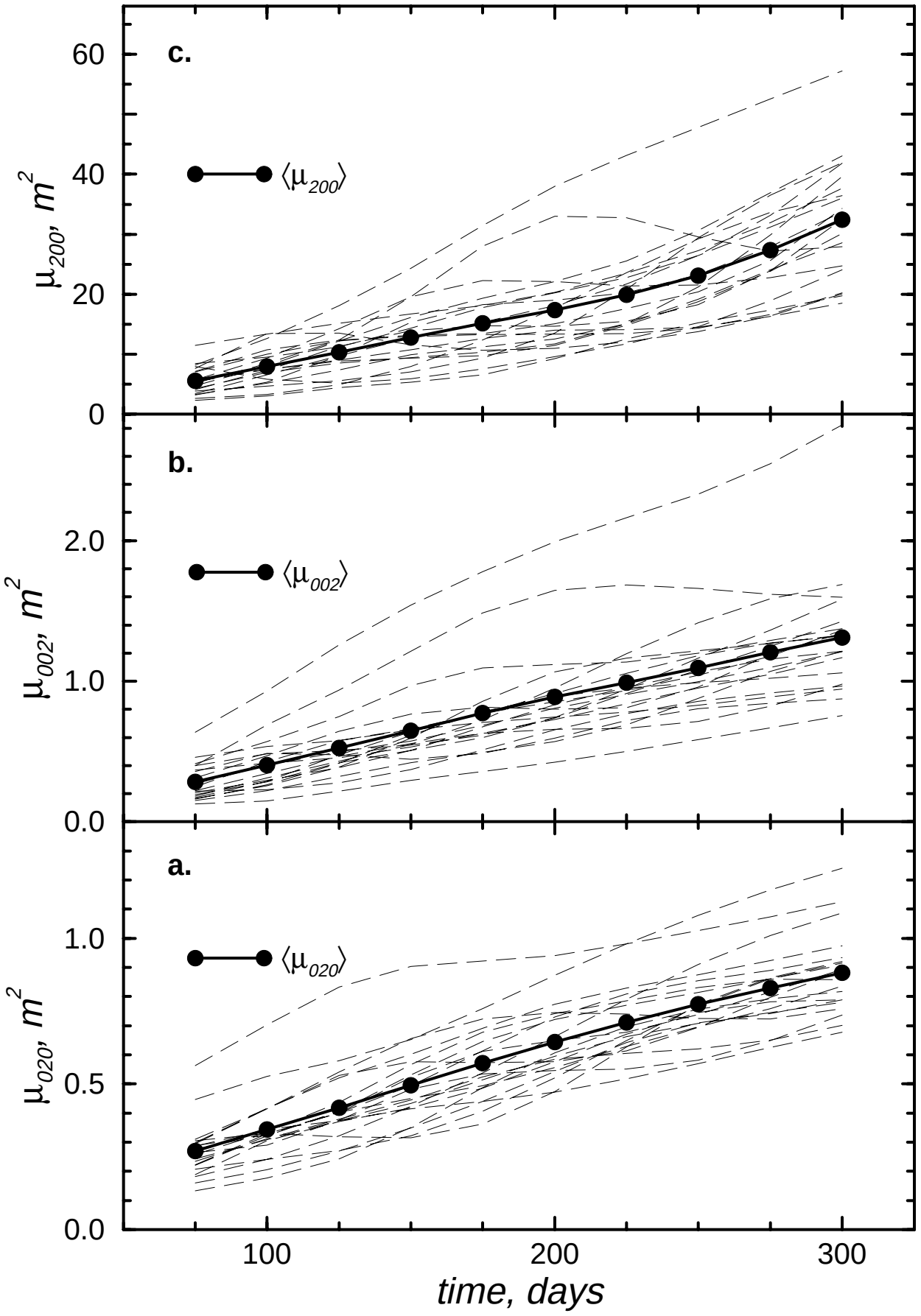
c.
b.
a.
⟨μ200⟩
⟨μ002⟩
⟨μ020⟩
μ200, m2
μ002, m2
μ020, m2
60
40
20
0
2.0
1.0
0.0
1.0
0.5
0.0
100
200
300
time, days

Figure 12

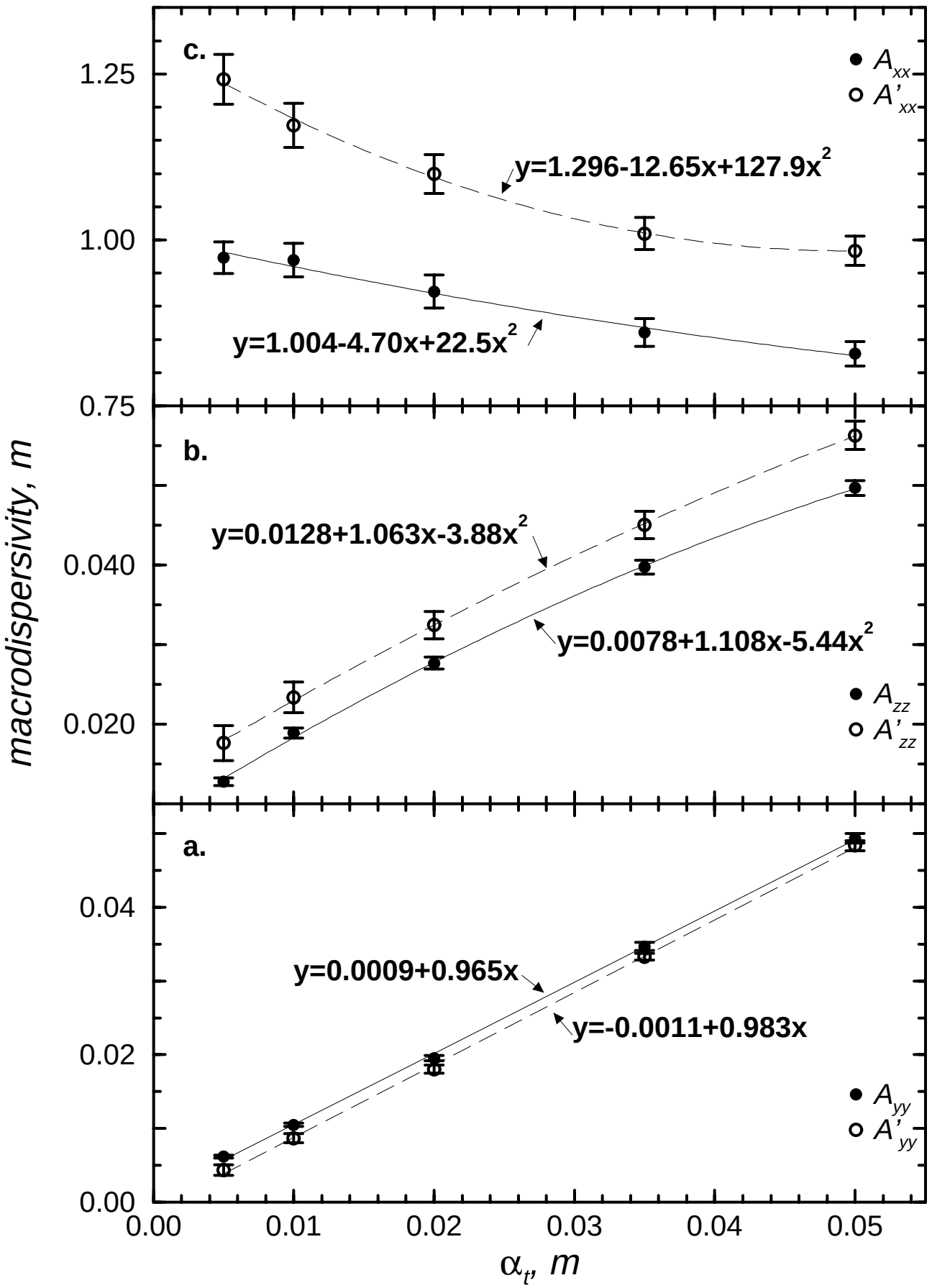
c.
b.
a.
A_{xx}
A'_{xx}
A_{zz}
A'_{zz}
A_{yy}
A'_{yy}
y=1.296-12.65x+127.9x²
y=1.004-4.70x+22.5x²
y=0.0128+1.063x-3.88x²
y=0.0078+1.108x-5.44x²
y=0.0009+0.965x
y=-0.0011+0.983x
1.25
1.00
0.75
0.040
0.020
0.04
0.02
0.00
0.00
0.01
0.02
0.03
0.04
0.05
macrodispersivity, m
α_t, m

Figure 13

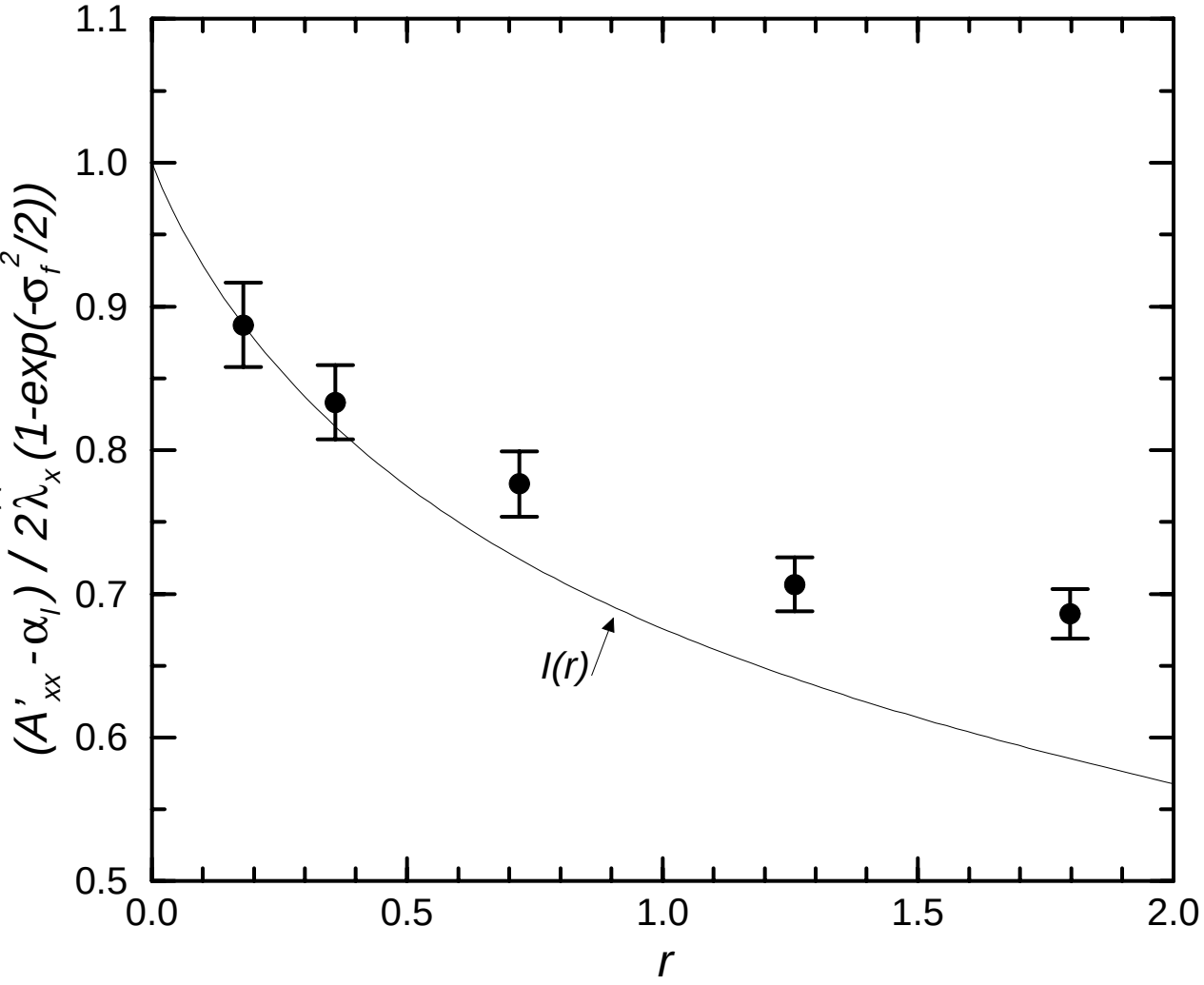

Figure 14

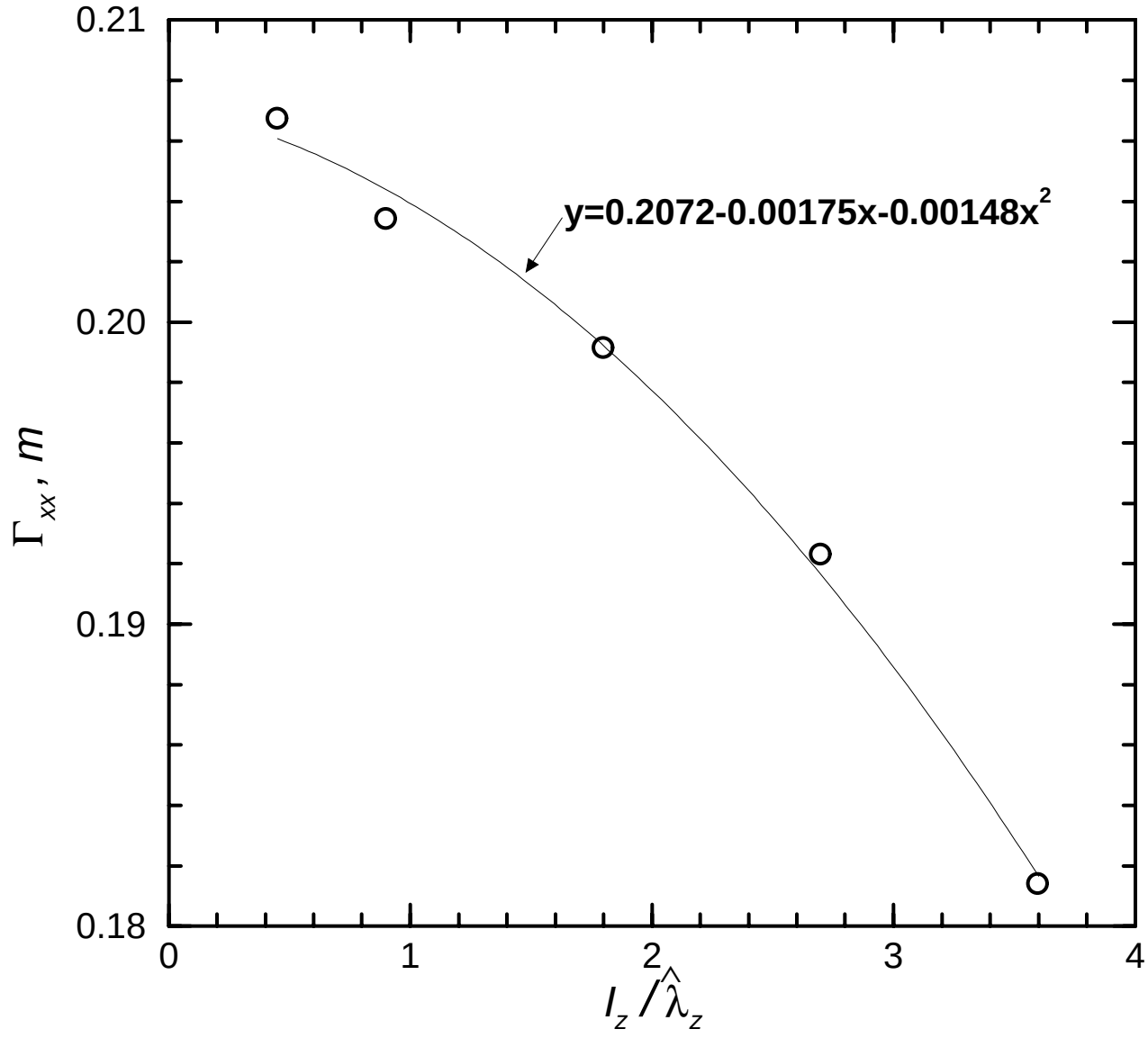
0.21
0.20
0.19
0.18
0
1
2
3
4
Γ_{xx}, m
$I_z / \hat{\lambda}_z$
y=0.2072-0.00175x-0.00148x^2

Figure 15

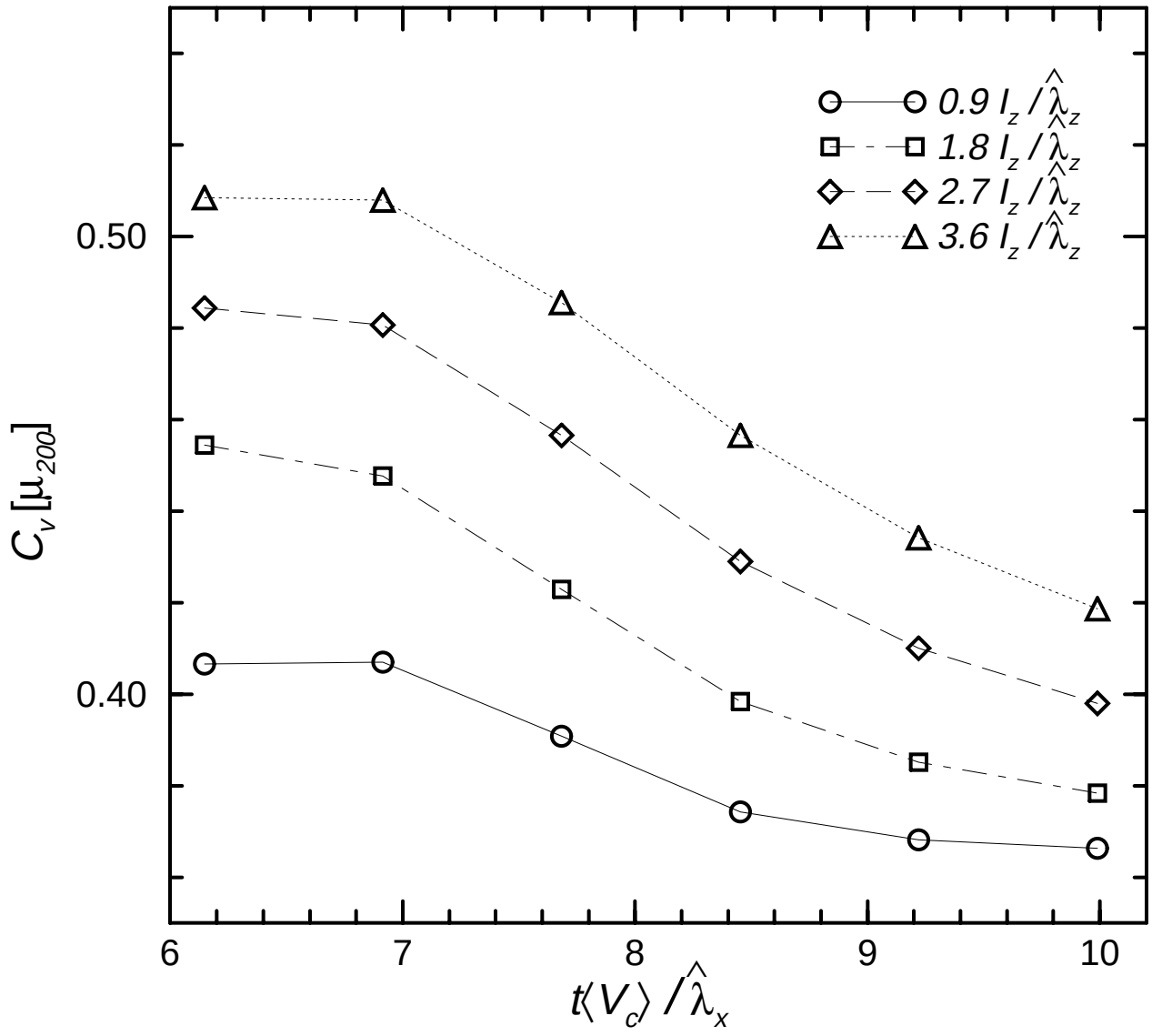
0.9 $l_z / \hat{\lambda}_z$
1.8 $l_z / \hat{\lambda}_z$
2.7 $l_z / \hat{\lambda}_z$
3.6 $l_z / \hat{\lambda}_z$
0.50
0.40
C_v [μ_{200}]
6
7
8
9
10
$t\langle V_c \rangle / \hat{\lambda}_x$

Figure 16

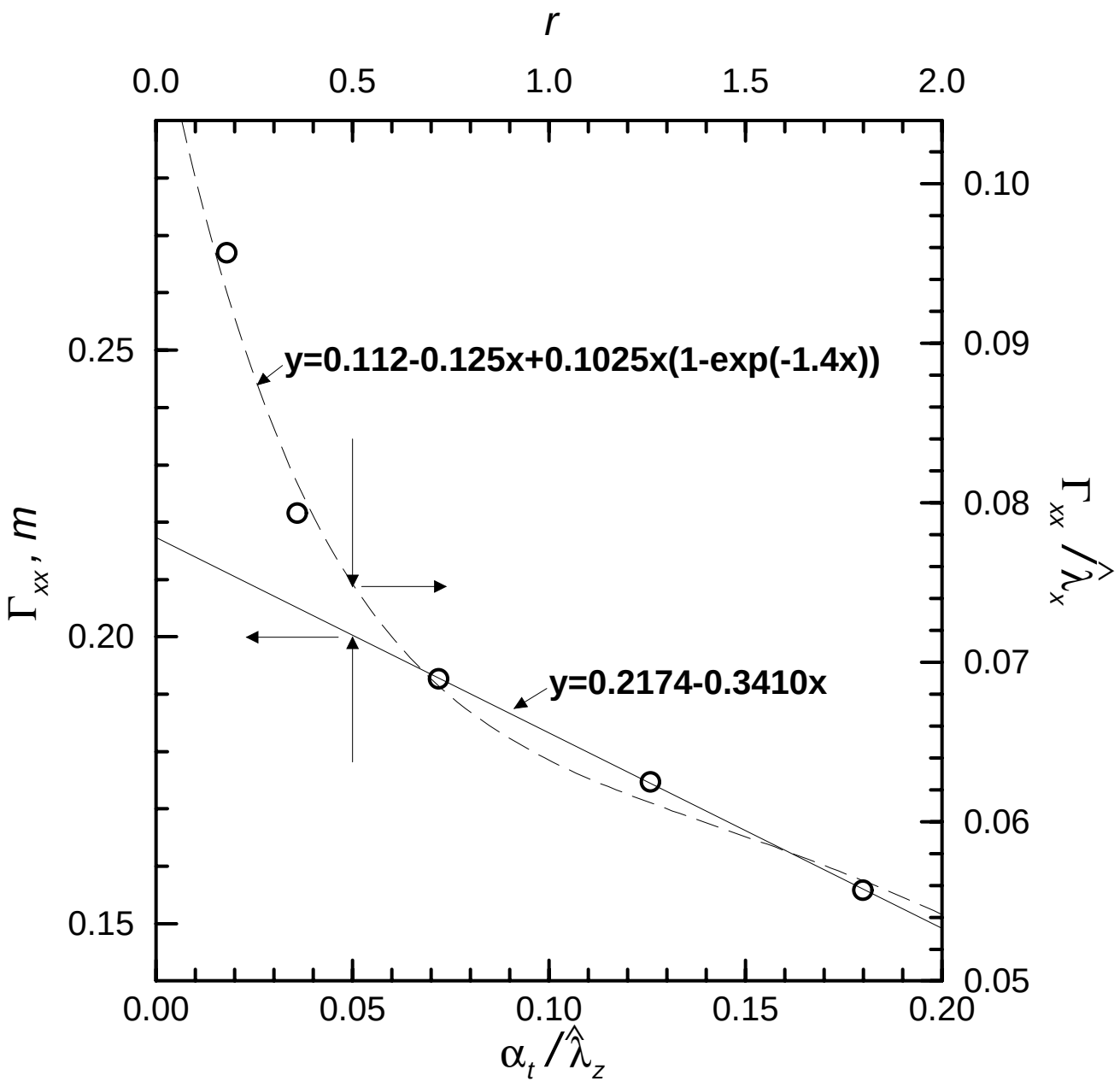
r
0.0
0.5
1.0
1.5
2.0
0.25
0.20
0.15
0.10
0.09
0.08
0.07
0.06
0.05
0.00
0.05
0.10
0.15
0.20
y=0.112-0.125x+0.1025x(1-exp(-1.4x))
y=0.2174-0.3410x
Γxx, m
Γxx / λ̂x
αt / λ̂z

Figure 17

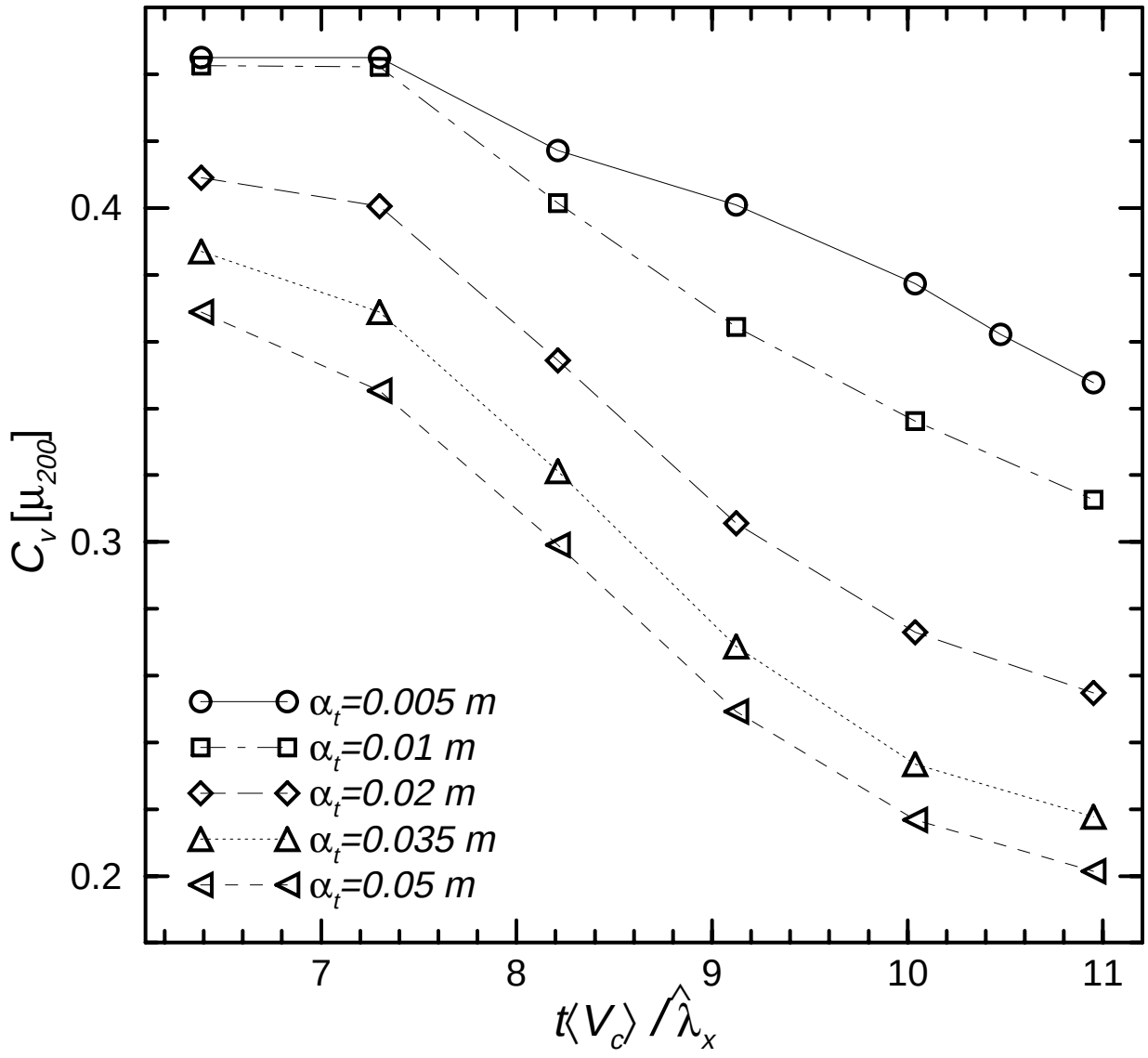
0.4
0.3
0.2
$C_v[\mu_{200}]$
7
8
9
10
11
$t\langle V_c\rangle / \hat{\lambda}_x$
α_t=0.005 m
α_t=0.01 m
α_t=0.02 m
α_t=0.035 m
α_t=0.05 m

Figure 18

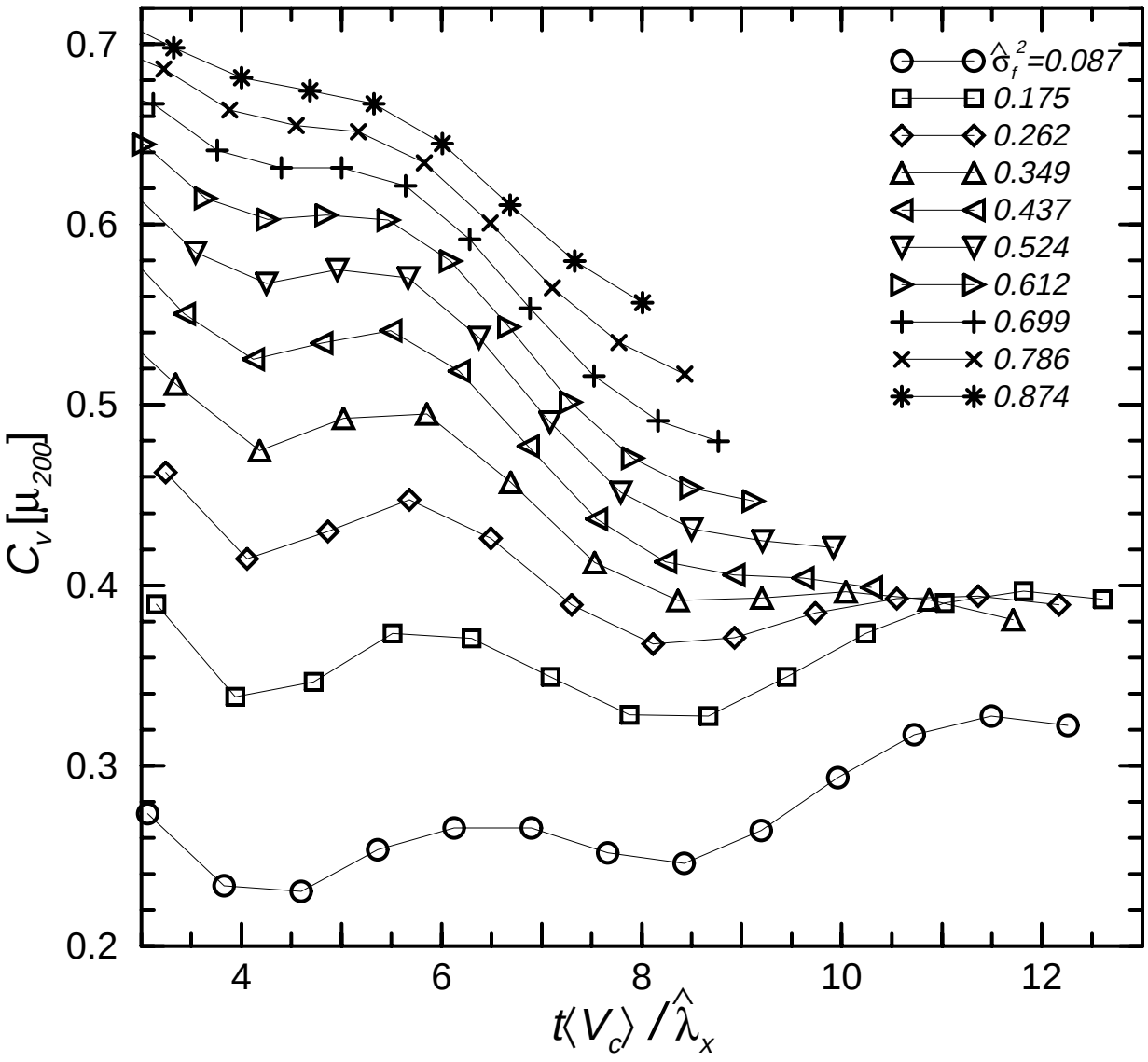
0.7
0.6
0.5
0.4
0.3
0.2
4
6
8
10
12
$C_v\,[\mu_{200}]$
$t\langle V_c\rangle\,/\,\hat{\lambda}_x$
$\hat{\sigma}_f^2$=0.087
0.175
0.262
0.349
0.437
0.524
0.612
0.699
0.786
0.874

Figure 19

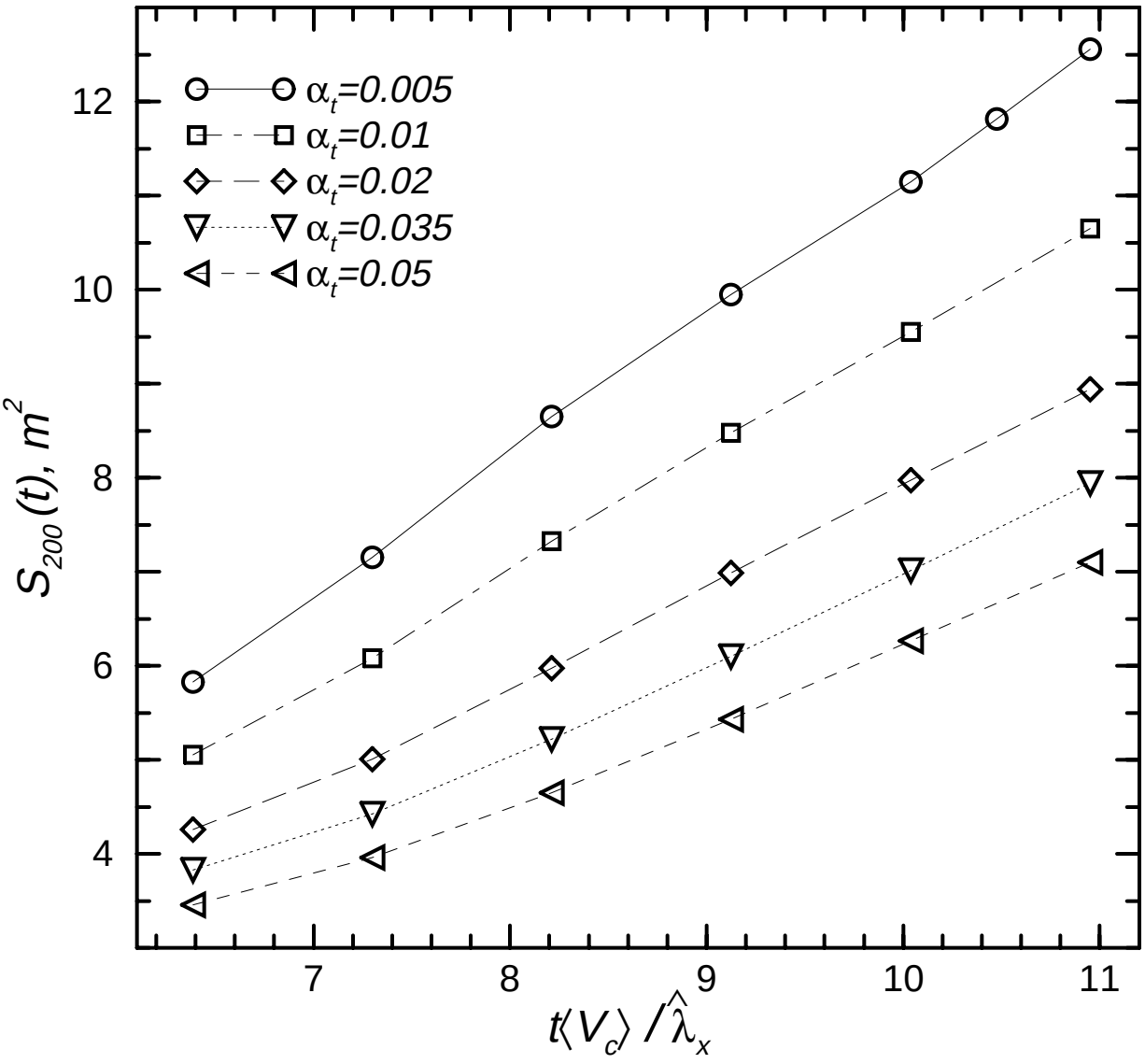
α_t=0.005
α_t=0.01
α_t=0.02
α_t=0.035
α_t=0.05
$S_{200}(t)$, m^2
$t\langle V_c\rangle / \hat{\lambda}_x$
4
6
8
10
12
7
8
9
10
11

Figure 20

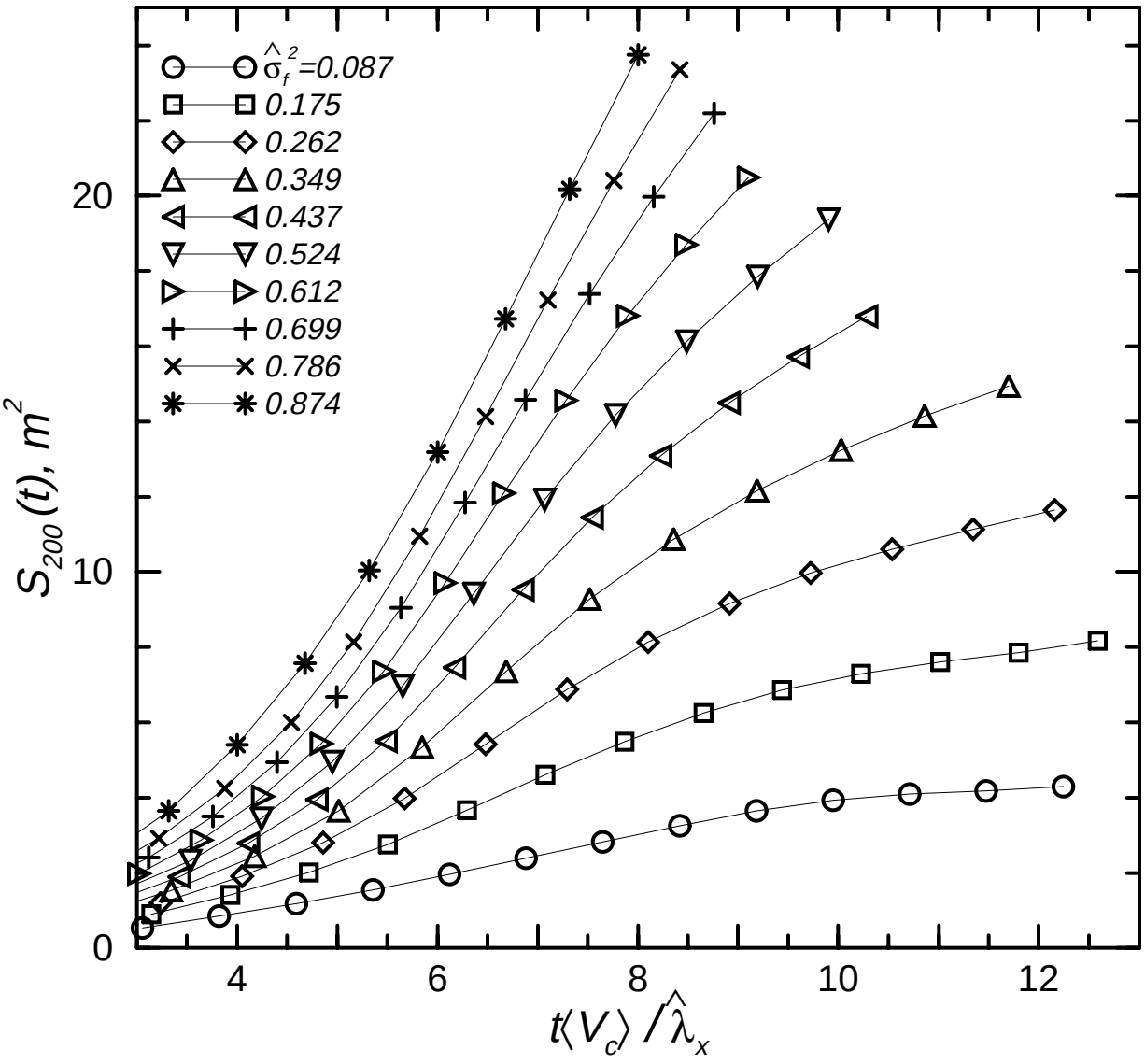
$\hat{\sigma}_f^2$=0.087
0.175
0.262
0.349
0.437
0.524
0.612
0.699
0.786
0.874
$S_{200}(t)$, m^2
0
10
20
4
6
8
10
12
$t\langle V_c\rangle / \hat{\lambda}_x$

Figure 21

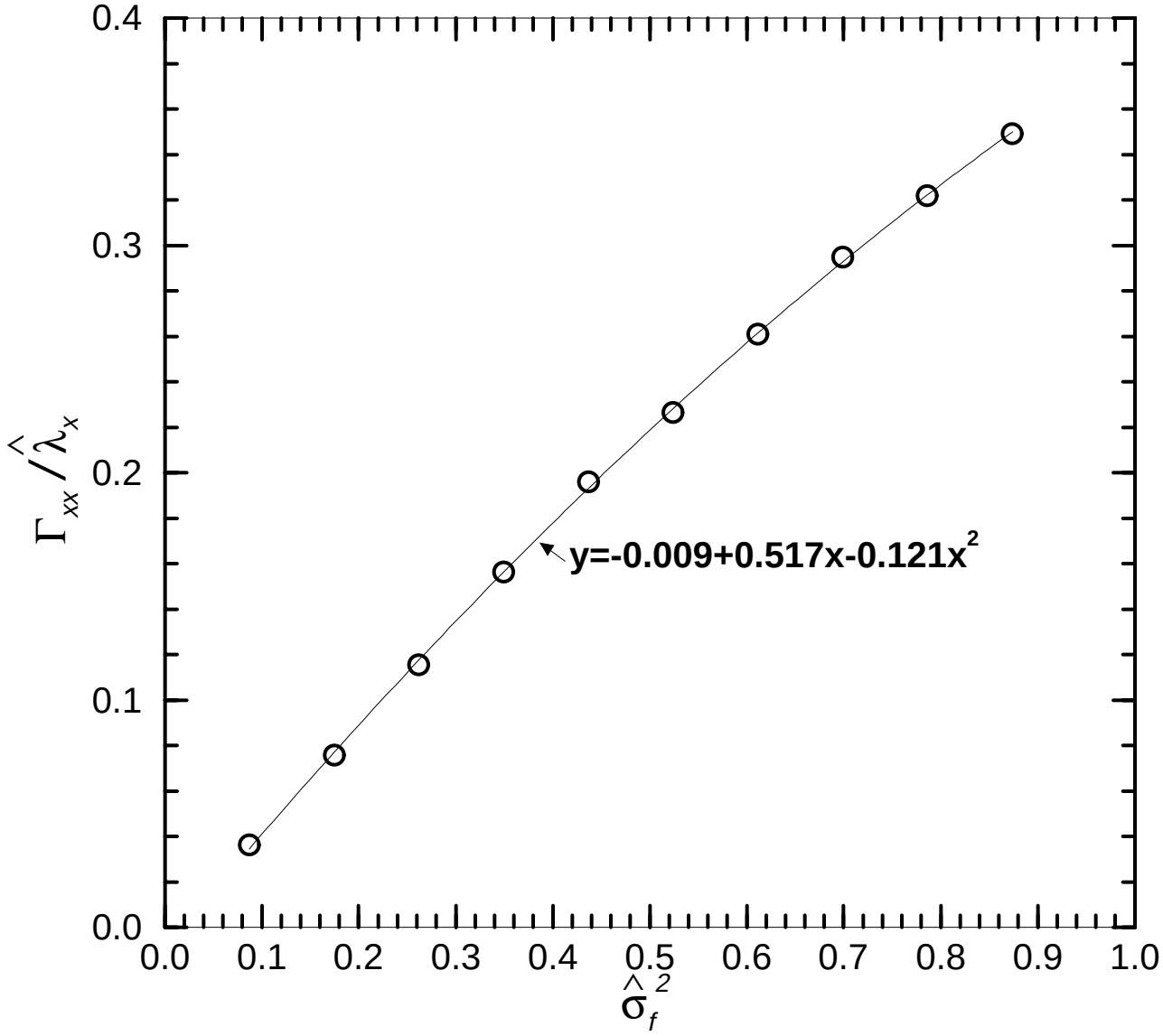
0.4
0.3
0.2
0.1
0.0
$\hat{\Gamma}_{xx}/\hat{\lambda}_x$
y=-0.009+0.517x-0.121x^2
0.0
0.1
0.2
0.3
0.4
0.5
0.6
0.7
0.8
0.9
1.0
$\hat{\sigma}_f^2$

Figure 22

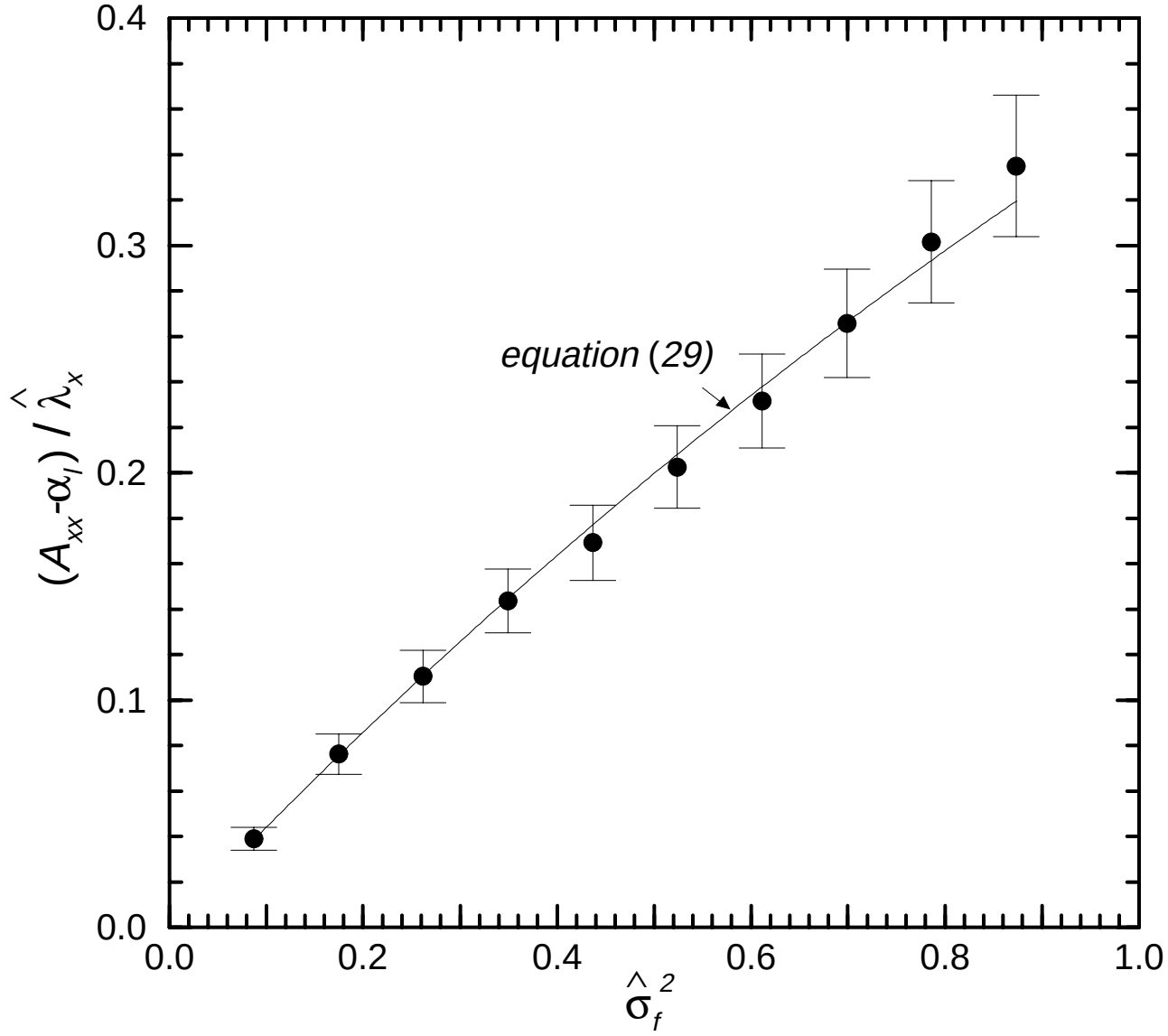
0.4
0.3
0.2
0.1
0.0
0.0
0.2
0.4
0.6
0.8
1.0
$(A_{xx}-\alpha_l) / \hat{\lambda}_x$
$\hat{\sigma}_f^2$
equation (*29*)

Figure 23

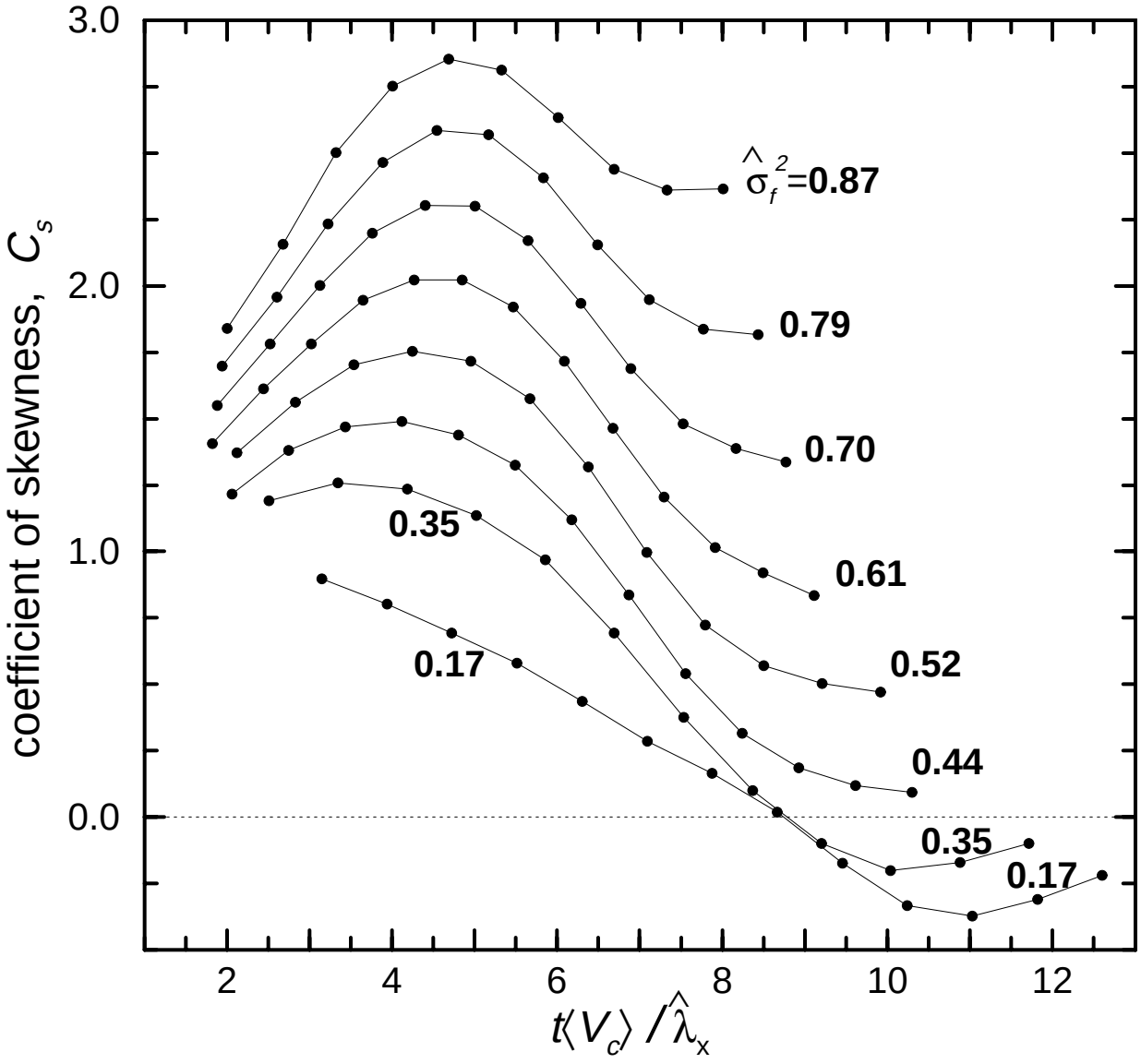
3.0
2.0
1.0
0.0
coefficient of skewness, C_s
2
4
6
8
10
12
$t\langle V_c\rangle / \hat{\lambda}_x$
$\hat{\sigma}_f^2$=0.87
0.79
0.70
0.61
0.52
0.44
0.35
0.17
0.35
0.17

Figure 24

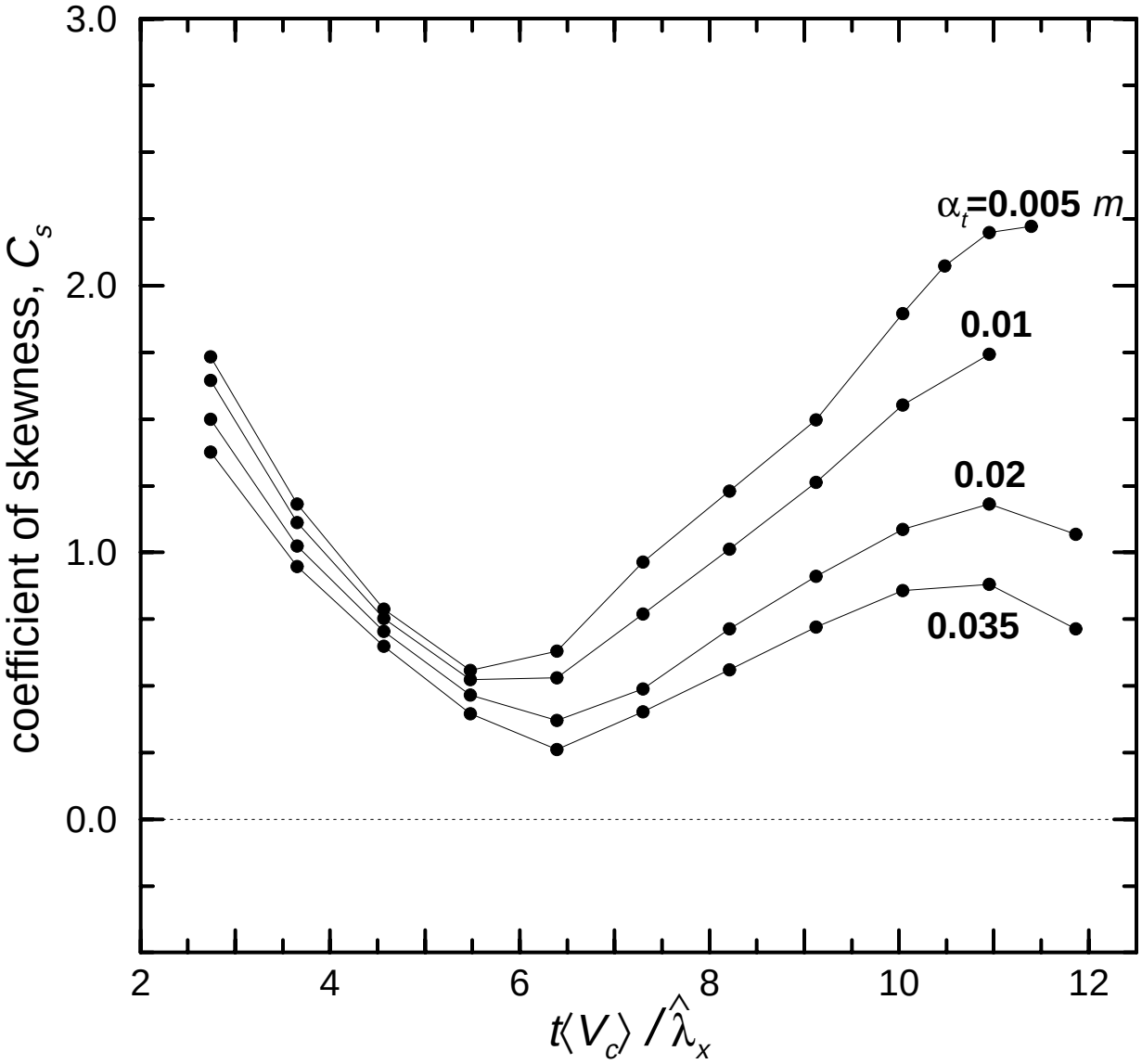
3.0
2.0
1.0
0.0
2
4
6
8
10
12
coefficient of skewness, C_s
$t\langle V_c\rangle / \hat{\lambda}_x$
α_t=0.005 m
0.01
0.02
0.035